

AD-A041 486

HULL UNIV (ENGLAND) DEPT OF APPLIED PHYSICS
INTERACTION OF PULSED CO₂ AND PULSED HF/DF LASER RADIATION WITH--ETC(U)
FEB 77 B K DEKA, P E DYER, D J JAMES

F/6 20/5

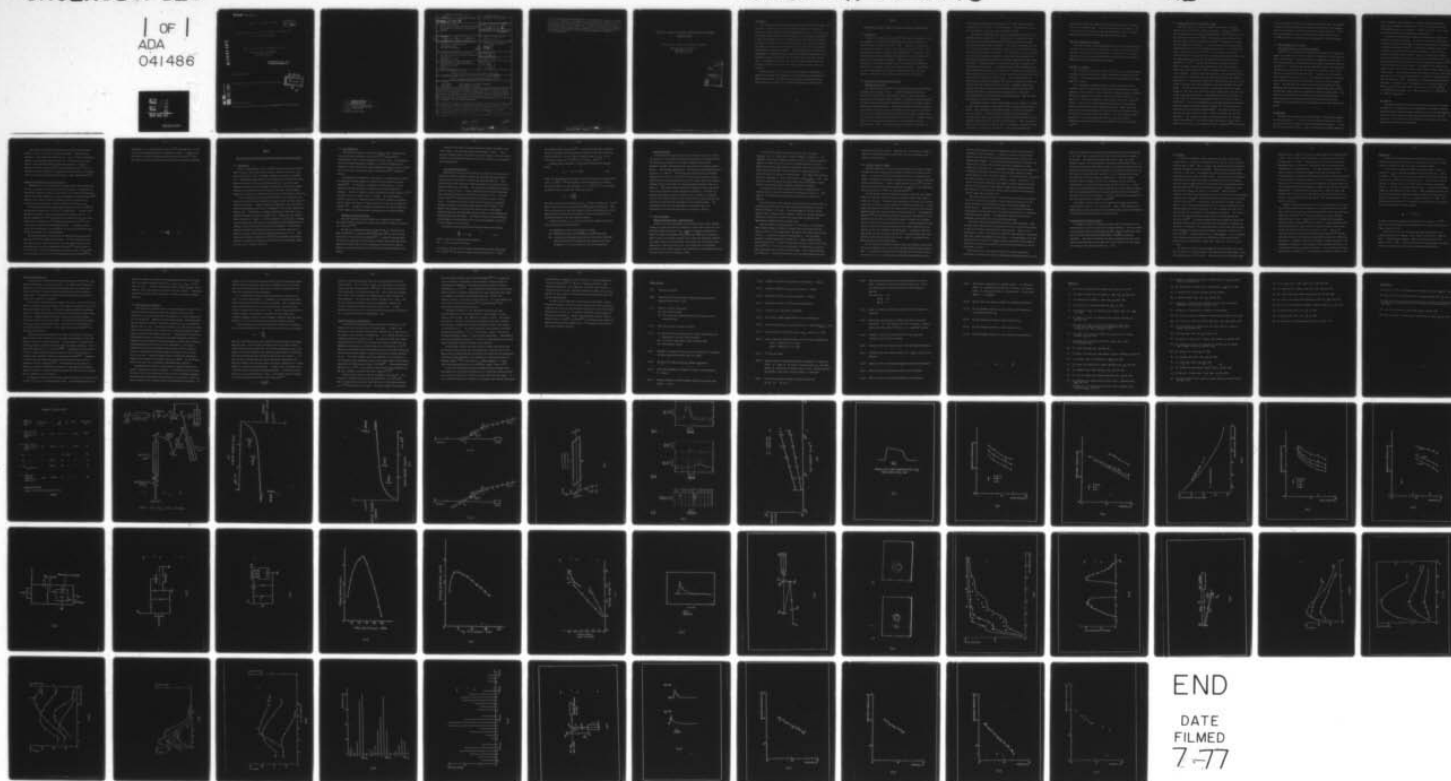
AF-AFOSR-2610-74

UNCLASSIFIED

AFOSR-TR-77-0778

NL

1 OF 1
ADA
041486



END

DATE
FILMED
7-77

AFOSR-TR- 77 - 0778

BOARD GRANT: AFOSR - 74 - 2610

12

Interaction of pulsed CO₂ and pulsed HF/DF laser radiation with
gaseous and solid targets

Principal Investigator: Professor S.A. Ramsden

Department of Applied Physics,
University of Hull,
Hull, HU6 7RX, U.K.

Approved for public release;
distribution unlimited.

1st February, 1977.

Final Report: 1st October, 1973 - 31st August, 1976.



Prepared for U.S.A.F.

and European Office of Aerospace Research and Development, London, England.

AU NO. _____
DDC FILE COPY

ADA 041486

AIR FORCE OFFICE OF SCIENTIFIC RESEARCH (AFSC)
NOTICE OF TRANSMITTAL TO DDC
This technical report has been reviewed and is
approved for public release IAW AFR 190-12 (7b).
Distribution is unlimited.
A. D. BLOSE
Technical Information Officer

19 REPORT DOCUMENTATION PAGE		BEFORE COMPLETING FORM
1. Report Number AFOSR-TR- 77- 0778	2. Govt Accession No.	3. Recipient's Catalog Number
4. Title (and Subtitle) INTERACTION OF PULSED CO₂ AND PULSED HF/DF LASER RADIATION WITH GASEOUS AND SOLID TARGETS.	5. Type of Report & Period Covered Final Scientific <i>rept.</i> 1 Oct 1973 - 31 Aug 1976	
6. Performing Org. Report Number		
7. Author(s) B. K. Peka, P. E. Dyer, D. J. James and S. A. Ramsden	8. Contract or Grant Number AFOSR-74-2610 <i>new</i>	
9. Performing Organization Name and Address Department of Applied Physics University of Hull Hull HU6 7RX, England	10. Program Element, Project, Task Area & Work Unit Numbers 61102F <i>17</i> 9767-04 <i>16</i>	
11. Controlling Office Name and Address Air Force Office of Scientific Research/NP Bolling AFB Washington, DC 20332	12. Report Date 11 1 Feb 1977	
14. Monitoring Agency Name and Address European Office of Aerospace Research and Development/LNP Box 14 FPO New York 09510	13. Number of Pages 75	
15. 12 77 p.		
16. & 17. Distribution Statement Approved for public release; distribution unlimited.		
18. Supplementary Notes 15 ✓ AF-HFOSR-2610-74		
19. Key Words HF/DF LASERS LASER INDUCED ATMOSPHERIC BREAKDOWN CO₂ LASERS LASER TARGET INTERACTION		
20. Abstract: HF and DF laser radiation from an unstable resonator was used to study laser induced breakdown in air, nitrogen and argon. For air at a pressure of 760 torr a threshold of 5×10^{10} watts/cm ² was found for HF radiation induced breakdown. This threshold is proportional to $p^{-0.6}$. The breakdown threshold for pure Ar is 1.6×10^{10} watts/cm ² at atmospheric pressure and scales to the -0.95 power with pressure. The threshold for DF laser induced breakdown of air was twice the threshold of HF laser induced breakdown. The interaction of carbon targets with pulsed CO ₂ laser radiation was studied. The pulse width was 5 nanoseconds and the maximum flux density ranged from 4×10^{10} to 5×10^{12} watts/cm ² . The ion expansion velocity, electron temperature and x-ray emission from the carbon surface were measured. X-ray continuum emission was only detected at the highest flux densities, $> 10^{12}$ watts/cm ² , when an effective electron temperature of ~ 1 keV was measured. [Continued on reverse]		

FORM 1473

400996

The laser induced breakdown thresholds for Ar, N₂ and CO₂ were measured using CO₂ laser pulses of length 3 to 40 nanoseconds. In argon the threshold becomes energy dependent for pulse length less than 5 nanoseconds and is power dependent for pulse lengths greater than 14 nanoseconds. A similar transition between energy and power dependence is also exhibited in nitrogen. In a mixture of CO₂/N₂/He the threshold for laser induced breakdown exhibited a pressure dependence of $p^{-0.3}$ for 3 nanosecond pulses. This is a weaker pressure dependence than observed in previous experiments.

He - 0.3 p^{-0.3}

Interaction of pulsed CO₂ and pulsed HF/DF radiation with gaseous
and solid targets

B.K. Deka, P.E. Dyer, D.J. James and S.A. Ramsden

Department of Applied Physics,
University of Hull,
Hull, HU6 7RX, U.K.

SECTION 1	
WFO	Write Section <input checked="" type="checkbox"/>
WFO	Soft Section <input type="checkbox"/>
UNANNOUNCED	<input type="checkbox"/>
NOTIFICATION	
DISTRIBUTION/AVAILABILITY CODE	
DISC.	ASAPL and/or SPECIAL
A	

Introduction

This final report, which covers the period 1st October 1973 - 31st August 1976, deals with an experimental investigation into the interaction of high power molecular gas laser radiation with solid and gaseous targets. In the first part of the report the development of a short pulse (\sim few nanosecond) and long pulse (\sim 60ns) $10.6\mu\text{m}$ CO_2 laser system is described and the results of an investigation into plasma production from solid targets reported. Measurements of breakdown thresholds in various gases of interest were also made at $10.6\mu\text{m}$ and the pulse width dependence of breakdown studied. In the second part of the report the development of a pulsed HF/DF laser is described, along with the results of gas breakdown threshold measurements in Ar, N_2 and air which were made using this laser. A comprehensive study of mode control using an unstable resonator on the high gain HF/DF laser was also made and the results of these studies are discussed.

The work carried out in the first part of the report was undertaken on contract number AFOSR-74.2610 under the title 'Interaction of pulsed CO_2 laser radiation with gaseous and solid targets' and in the second part under the title 'Interaction of HF/DF laser radiation with gaseous and solid targets'.

PART I

Interaction of pulsed CO₂ laser radiation with gaseous and solid targets

1.1 Introduction

A short pulse TEA CO₂ laser oscillator⁽¹⁾ operating at atmospheric pressure was developed to investigate the amplification of nanosecond pulses in an amplifier chain with small signal gain of 10^6 . Measurements of the energy extraction efficiency were made to study rotational saturation effects; the problem of inter-stage isolation was also investigated. Peak powers > 1 GW have been achieved with 3ns pulses and problems associated with focusing this power onto a solid target investigated. The system was used to measure thresholds for dielectric breakdown in gases for various pulse lengths and pressures and to generate plasmas from solid carbon targets. An oscillator was also developed and used to study the interaction of relatively long duration (~ 60ns) high intensity 10.6μm radiation with solid targets.

1.2 CO₂ laser system design and development

Nanosecond pulse system

The experimental configuration of the complete nanosecond pulse oscillator-amplifier system is shown in Fig 1. A double discharge oscillator and electro-optic switch⁽¹⁾ was used to generate either a square pulse with a risetime \lesssim 1ns and variable duration (3-50ns) or a single 2ns mode-locked pulse. The type of pulse was selected by varying the gas mixture in a Brewster angle NaCl gas cell inside the cavity. A 2mm thick Ge plate at Brewster's angle was positioned between the oscillator and the GaAs switch to assist in decoupling the laser cavity formed around the amplifiers by the oscillator output mirror and target back-reflection when the switch was not activated. A further Brewster angle Ge plate after the switch provided a reflection analyser of high discrimination ($> 10^3$). Both the preamplifier and the main amplifier were

excited using a double-discharge configuration⁽²⁾, these amplifiers having apertures of $4 \times 4 \text{ cm}^2$ and $5 \times 5 \text{ cm}^2$ respectively. The single pass gain, G , of the preamplifier was 10 and of the main amplifier, 10^4 .

The results of amplifying square pulses of variable duration in the main amplifier alone are shown in Fig 2. The full line is a theoretical curve calculated from the Frantz-Nodvik theory⁽³⁾ modified to take into account divergence of the beam along the amplifier. We assume a saturation parameter of 150 mJ.cm^{-2} corresponding to complete extraction of the rotational levels but with the lower vibrational level frozen. For short pulses ($< 10 \text{ ns}$) we see that the output energy density is reduced due to rotational freezing whereas for 20 ns pulses the output energy density is increased, probably due to lower level relaxation. Using these results a suitable pre-amplifier was designed and incorporated into the system. The additional gain ($\times 10^2$) introduced by the pre-amplifier necessitated the use of interstage isolation and a 2.5 cm gas cell filled with SF_6 at a pressure of 1.5 torr was used between the pre-amplifier and main amplifier to reduce pre-lasing effects. Since SF_6 only absorbs the P14-P26 lines of the $10.4 \mu \text{ CO}_2$ band an NaCl prism was included to restrict any oscillation of the amplifier chain to this band. Preliminary experiments indicated that the cell reduced pre-lasing effects significantly while still allowing the efficient transmission of nanosecond pulses. Using this amplification system, 3 ns duration pulses with output powers $> 1 \text{ GW}$, and a beam divergence of 0.4 mrad were generated.

An improved polarizer-analyser configuration was also studied in an attempt to improve the de-coupling of the amplifier chain from the oscillator output mirror. This used two Brewster's angle Ge plates in reflection arranged as shown in Fig 3(a). It can be seen that, except when the GaAs switch is activated, both planes of polarization of amplified spontaneous emission in the amplifier chain will be lost from the system (Fig 3(b)). Thus, if residual birefringence in the GaAs crystal is small, pre-lasing does not occur even when the output is focused onto a solid target. Also, the system gives good

discrimination between the transmitted signal when the switch is activated to that in the unswitched state. Using this configuration laser energies $\sim 6\text{J}$ in a 3ns pulse were obtained on target with approximately 0.5J in a prepulse and without the need for the prism and SF_6 cell described above.

Long pulse (60ns) laser oscillator

To obtain relatively long duration (60ns) pulses at high energy levels the main amplifier was operated as an oscillator, the cavity consisting of a plane gold coated Zr-Cu mirror and an NaCl etalon, separated by 6.5m . The system was apertured to give near single transverse mode operation and peak powers of 300MW achieved with a beam divergence of 1 mrad .

Oscillator development

The mode-locked oscillator described in section 2.1 used a stable resonator and TEM_{00} operation was ensured by placing a 6mm diameter aperture within the resonator. This, however, severely limited the mode-volume and thus the output power of the device.

It is advantageous in many applications to use a more powerful drive oscillator since this necessitates a lower overall amplifier gain for a given output power of the system. We have developed an unstable resonator oscillator which may be operated to give either a train of mode-locked pulses of 3ns duration or a single axial mode pulse using an SF_6 -He cell in the resonator⁽⁴⁾ (Fig 4). With a $5 \times 5 \times 100\text{ cm}^3$ double-discharge system we have produced trains of mode-locked pulses (3ns FWHM) with peak power $\sim 300\text{MW}$, and single axial mode pulses with peak powers of 14MW , both substantially greater than can be achieved with a conventional stable resonator. We have investigated the propagation of the annular output beam and shown that after suitable transformation using spatial filters it is suitable for driving an amplifier chain⁽⁴⁾.

1.3 Plasma production from solid carbon targets

Both laser systems were used in a study of the properties of plasma produced by the irradiation of plane carbon targets. Previous work^(5,6,7) with the 60ns CO₂ laser oscillator at flux densities of $4 \cdot 10^{11} \text{ W.cm}^{-2}$ showed that the plasma had a low reflectivity⁽⁵⁾ ($< 10\%$) and that a small fraction of the electrons had an effective temperature of $\sim 2 \text{ keV}$ ⁽⁶⁾ in contrast to an average electron temperature of 100-150eV. A possible explanation is that non-linear absorption processes are occurring during the interaction. It was also shown that, at the low critical density (10^{19} cm^{-3}) of the interaction, thermal conduction plays an important role, increasing the plasma dimensions and leading to a weak dependence of asymptotic ion expansion velocity with laser flux density⁽⁷⁾ ($v \sim \phi^{0.12}$). With 60ns duration pulses a steady-state density profile can evolve and we have now extended some of these measurements to shorter laser pulses during which there is insufficient time to set-up steady-state conditions. Using the single mode oscillator a 5ns rectangular pulse was selected with the electro-optic gate and amplified by the high gain amplifier system (Fig 1). The laser pulse shape after amplification is shown in Fig 5(a) in which five pulses have been superimposed to show the reproducibility of the system. The radiation was focused onto a tilted carbon target in a vacuum chamber ($p \sim 10^{-5} \text{ torr}$) with an f/10, 25cm focal length, plano convex NaCl lens to give a spot diameter of $140 \mu\text{m}$. The maximum flux density at the target was $5 \cdot 10^{12} \text{ W.cm}^{-2}$ and calibrated CaF₂ attenuators were used to range this down to $4 \cdot 10^{10} \text{ W.cm}^{-2}$. A pair of X-ray detectors were arranged symmetrically about the plasma to monitor the continuum emission and metal foil filters were used to determine the effective electron temperature⁽⁸⁾. The signal from the X-ray detectors (Fig 5(b)) lasts for $\sim 10 \text{ ns}$ - significantly longer than the laser pulse length. Ion expansion velocities were measured using a pair of biased Faraday cup collectors. The ion probe signals are shown in Fig 5(c) and at the maximum flux used in these experiments no fast ion component⁽⁹⁾ was observed.

Figure 6 shows the variation of ion expansion velocity with laser flux density; by comparison with the steady state situation the ion velocity (and therefore the electron temperature) increases more rapidly with flux density ($v \sim \phi^{0.2}$). X-ray continuum emission was only detected at the highest flux densities ($\sim 10^{12} \text{ W.cm}^{-2}$) when an effective electron temperature of $\sim 1 \text{ keV}$ was measured.

1.4 Gas breakdown studies at $10.6 \mu\text{m}$

Pulse width dependence of breakdown thresholds

Smith⁽¹⁰⁾ has reported breakdown threshold measurements for TEA CO_2 laser pulses in Ar which indicate that the threshold is independent of pulse width for pulses $> 50 \text{ ns}$ duration. We have extended his measurements to pulse widths in the range $3\text{-}40 \text{ ns}$ using the single axial mode oscillator, electro-optic gate and pre-amplifier. In order to preserve the approximately square laser pulse shape the output power was limited to 10 MW and the pulse length to $\sim 40 \text{ ns}$ so that amplifier saturation effects were not severe. A typical pulse shape used in these measurements is shown in Fig 7. The radiation was focused in a pressure cell, containing the gas under investigation, with an $f/5$, 5 cm focal length mirror. The laser power was varied using calibrated polyethylene and CaF_2 attenuators and the threshold for breakdown was defined as the power at which the inclusion of a 20% attenuator extinguished the visible breakdown spark. The laser power at threshold was calculated from the measured pulse shape and pulse energy and the focal spot radius calculated from the measured beam divergence of 1.4 mrad (FWHM) after the preamplifier and the focal length of the mirror.

Ar Thresholds

Thresholds were measured in Ar for pulses $3\text{-}40 \text{ ns}$ in duration and pressures in the range $20\text{-}740 \text{ torr}$. The variation of breakdown threshold power density, P_{th} , with pulse width is shown in Fig 8 for three different pressures. In each case it is seen that for pulses $\leq 5 \text{ nsec}$ the threshold power density exhibits an

inverse dependence with pulse width, τ , such that the energy threshold, $E_{th} (= P_{th}\tau)$, approaches a steady value. Thus in this short pulse regime the threshold becomes energy dependent. However, for pulses $> 14\text{ns}$ a trend can be discerned towards a constant power characteristic.

In Fig 9 the threshold power density has been plotted as a function of pressure for various pulse widths. The slope of the lines is approximately - 0.5 which it should be noted does not agree with the theory for recombination or diffusion dominated breakdown⁽¹¹⁾; also elastic collisional losses are negligible at the pressures used in these experiments so that this cannot explain the observed pressure scaling. However, a possible loss mechanism may lie the production of excited states and in order to investigate this the measured thresholds have been compared with those computed by Rockwood et al⁽¹²⁾, in the presence of excitational losses. The results of this comparison are shown in Fig 10, where the experimental points have been plotted against pressure \times pulse length. The experimental points consistently lie above the theoretical curve and this may be due to diffusion which is neglected in the quantum-kinetic model of Rockwood et al⁽¹²⁾. Nevertheless, the agreement between experiment and theory is reasonably good. For example, for $\tau = 3\text{ns}$ and a pressure of 760 torr the experimental and theoretical values are $3.3 \times 10^{10} \text{ W.cm}^{-2}$ and $1.3 \times 10^{10} \text{ W.cm}^{-2}$ respectively; at $p = 120$ torr these are $8.2 \times 10^{10} \text{ W.cm}^{-2}$ and $6 \times 10^{10} \text{ W.cm}^{-2}$ respectively.

N₂ thresholds

The measured thresholds in Ar discussed in the previous section indicate the importance of excitational losses in determining the breakdown threshold. In molecular gases such losses would be expected to play an even more important role due to the availability of many levels below the ionisation level⁽¹³⁾. To investigate this, thresholds in research grade N₂ were measured in the range 3-40ns and at pressures from 100-700 torr.

Fig 11 shows the threshold power density as a function of pulse width while in Fig 12 it is shown as a function of pressure. The pulse width dependence is not unlike that obtained for Ar. For $\tau \leq 10$ nsec the threshold exhibits a constant energy behaviour while for $\tau > 20$ nsec a trend is seen towards a power dependent regime expected for long pulses. A pressure dependence for 3 nsec pulses of $p^{-0.3}$ is observed compared to $p^{-0.5}$ for Ar. The weaker pressure dependence is presumably due to an increase in excitational losses in N_2 as has been discussed previously for ~ 200 ns duration pulses⁽¹³⁾.

Breakdown thresholds for CO_2 laser gas mixtures

Breakdown of the laser medium imposes an upper limit on the maximum energy that can be extracted from high pressure CO_2 laser systems. Measurements of the breakdown threshold in CO_2 laser gas mixtures are therefore of considerable interest since these provide useful data for the design of high power devices⁽¹⁴⁾. Because of this interest threshold measurements were carried out using a 1/1/8: $CO_2/N_2/He$ mixture which is typical of that used in TEA CO_2 lasers.

For a gas pressure of 700 torr the measured threshold was $2.7 \times 10^{10} \text{ W.cm}^{-2}$ for 3ns duration pulses and $5 \times 10^9 \text{ W.cm}^{-2}$ for 20ns pulses. The pulse width dependence was similar to that observed for Ar and N_2 (Figs 8 and 11). A pressure dependence of $p^{-0.3}$ was obtained for 3ns duration pulses which can be compared with a dependence of $p^{-0.7}$ obtained by Berger and Smith⁽¹⁴⁾ using ~ 70 ns duration pulses and 5/1/1: $He/CO_2/N_2$ mixtures. The weaker pressure scaling in our measurements is presumably due to increased excitational losses for the short pulses used in the experiments.

The energy thresholds at 700 torr for 3ns and 20ns duration pulses were found to be 81 J/cm^2 and 100 J/cm^2 respectively. If these thresholds, which were obtained using $\sim 100 \mu\text{m}$ diameter spot size, are scaled according to the previously measured spot size dependence of threshold⁽¹⁴⁾ reduced values of $\sim 6 \text{ J.cm}^{-2}$ and $\sim 7 \text{ J.cm}^{-2}$ are obtained for spot sizes $\geq 0.2 \text{ cm}$. These results can be compared with values of 10 J.cm^{-2} measured by Berger and Smith⁽¹⁴⁾ for

70ns pulses and $\sim 7 \text{ J.cm}^{-2}$ measured by Pan et al⁽¹⁵⁾ using 2ns pulses in each case for 5/1/1:He/CO₂/N₂ mixtures at atmospheric pressure. A comparison of our results with those predicted using the quantum kinetic model⁽¹⁶⁾ shows again that excited state production accounts well for the measured thresholds.

PART II

Interaction of pulsed HF/DF laser radiation with gaseous and solid targets.

2.1 Introduction

There is a considerable interest in HF/DF electrically initiated chemical lasers because of their high electrical-optical conversion efficiencies and because particularly for DF transitions, atmospheric absorption is extremely low. Although the highest energies and efficiencies have been obtained using high energy e-beams to initiate reactions between H_2 (or D_2) and F_2 , much information on such topics as atmospheric transmission and testing of optical components can be gained using lower energy systems which can be excited by producing a discharge in a mixture of H_2 (or D_2) and a fluorine donor such as SF_6 .

In this second phase of the project the objective was to study the interaction of pulsed HF/DF laser radiation with gaseous targets and solid targets in a gaseous background. In gases, of particular importance is the threshold for laser induced breakdown, since this is a fundamental limit to power transmission through a gas. Measurements of breakdown thresholds were thus made in air, nitrogen and argon using HF laser radiation ($2.6 - 3.0\mu m$) and in air using DF laser radiation ($3.6 - 4.0\mu m$). For this programme it was necessary to develop a suitable high power HF/DF laser for the breakdown threshold measurements and although initial efforts were directed towards developing a $\sim 10-20J$ system subsequent attention was diverted to the use of an unstable resonator on a compact and highly reliable discharge system giving energies of $\sim 1J$. With this system a focused intensity of $\sim 10^{11} W/cm^2$ was obtainable, this proving adequate for breakdown measurements in the $2.8\mu m$ and $3.8\mu m$ wavelength region, at least for gas pressures $\gtrsim 200$ torr.

2.2 Laser Development

Self-sustained discharge excitation of $\text{SF}_6\text{-H}_2$ or SF_6 - hydrocarbon gas mixtures has been obtained by various workers⁽¹⁷⁻¹⁹⁾ using electrode configurations similar to those developed for TEA CO_2 lasers. The generation of arc-free high energy density discharges is, however, considerably more difficult in this case due to the large attachment coefficient of SF_6 ($\sim 9.10^9\text{s}^{-1}\text{torr}^{-1}$) which makes the required degree of pre-ionization⁽²⁰⁾ difficult to achieve.

The problem has been overcome to some extent in 'double-discharge' systems by minimizing the delay between pre-ionization and initiation of the main discharge⁽¹⁸⁾. An alternative, and somewhat simpler approach, is to use resistively ballasted electrodes to stabilize the discharge against arc formation. The use of discrete resistive electrodes has enabled Pummer et al⁽¹⁷⁾ to obtain 10J HF laser pulses from a $\sim 6\lambda$ device. By using continuous resistive electrodes, a configuration potentially more suitable for producing uniform 'volume' discharges, it appears possible to improve the performance of the laser⁽²¹⁾. Because of the apparent advantages of this latter scheme our initial studies were directed towards constructing such resistive electrodes.

Continuous resistive electrodes

Resistive electrodes were constructed from a composition of styrene acrylonitrile (SAN) and graphite by compression moulding at 200°C and a pressure of $\sim 100\text{ KG.cm}^{-2}$ (22).

Our aim was to produce electrodes with resistivity of $\sim 10\Omega\text{cm}$ which has been reported to be an optimum value when discharge stability and the energy dissipated in the electrode are considered⁽²²⁾. A range of electrodes with various filler (graphite) concentrations was made and it was found that whilst mechanically strong samples could be produced with resistivities $\geq 100\Omega\text{cm}$, below this value the electrodes were extremely brittle and unsuitable for our purpose.

Electrical tests were carried out using several sample electrodes in the circuit shown in Fig 13 and the results are summarized in Table I. These show that although useful energy densities could be achieved with small volumes, scaling to larger discharge dimensions could only be achieved at the expense of input energy density.

u.v. pre-ionized discharges

Conditioning of TEA CO₂ laser discharges by irradiation with ultra-violet radiation has proved a powerful technique for producing high energy density discharges over a wide range of pressures and operating conditions. Some studies were therefore conducted to determine whether this technique could be applied to HF/DF laser excitation. The experimental arrangement and discharge circuit is shown in Fig 14. A 30cm x 2cm Bruce profiled aluminium electrode and a plane mesh electrode were used with a separation of ~ 1cm. A line of sliding sparks⁽²³⁾ situated beneath the mesh electrode was used as the u.v. source. The system was initially tested using a CO₂:N₂:He gas mixture and operated successfully at discharge energy densities up to ~ 200 J.l⁻¹ at⁻¹. However, when operated with SF₆:H₂:He gas mixtures over a wide range of parameters (pressure, discharge energy density, delay) it proved impossible to generate uniform glow discharges. The failure to achieve uniform discharges is attributed to the high electron loss rate through attachment to SF₆ which limits the degree of pre-ionization.

The electron density during the pre-ionization phase is described by

$$\frac{dn_e}{dt} = S - \beta n_e \quad \dots(1)$$

where S is the rate of photo-electron production,
and β is the attachment coefficient.

In the case of the CO₂ laser the minimum pre-ionization electron density must be $> 10^4 \text{ cm}^{-3}$ ⁽²⁰⁾ for uniform discharge initiation and values of $\sim 10^7 \text{ cm}^{-3}$

are probably achieved in practice⁽²⁴⁾. Since in the absence of an electric field the attachment rate in CO₂ laser gas mixtures is low, this density can build up during the $\sim 2\mu\text{s}$ delay which is normally used, i.e. $n_{eo} = \int S dt$. This implies a value of $S \sim 5.10^{12} \text{ cm}^{-3} \text{ s}^{-1}$ for $n_{eo} \sim 10^7 \text{ cm}^{-3}$.

In the case where attachment is significant, integration of equation 1 yields

$$n_e = S/\beta \{1 - e^{-\beta t}\} \quad \dots(2)$$

Taking the room temperature attachment coefficient of SF₆ at a pressure p(torr) to be $\beta \sim 9.10^9 p \text{ s}^{-1}$ (25) and assuming a similar production rate of photo-electrons to the case of CO₂ discharges i.e. $S \sim 5.10^{12} \text{ cm}^{-3} \text{ s}^{-1}$, we find that n_e rapidly reaches a steady state value, n_{eo} , given by

$$n_{eo} \sim \frac{5.10^{12}}{9.10^9 p}$$

For typical laser operating pressures of $P_{\text{SF}_6} = 40 \text{ torr}$, we obtain $n_{eo} \sim 10 \text{ cm}^{-3}$ which is well below the level required for conditioning the discharge. Thus, the u.v. sources must be much more intense than those used in CO₂ lasers and a delay between pre-ionization and initiation of the main discharge will be detrimental because of the short electron lifetime.

In order to develop a u.v. pre-ionized HF/DF laser further studies will have to be made of the following areas:

- (i) Development of fast, high current u.v. sources.
- (ii) Timing requirements between pre-ionizer and main discharge.
- (iii) Increasing the background ionization by the use of low ionization potential additives and reducing the SF₆ attachment coefficient by applying a d.c. bias field across the main discharge gap.

Resistor-pin laser

A resistively-ballasted pin laser was constructed using a matrix of 280 $1\text{K}\Omega$ resistors as the cathode and a plane aluminium plate as the anode (Fig 15). The electrodes were housed in a 1.2m long, evacuable lucite box with detachable Brewster's angle window mounts and provision for mounting internal mirrors. The electrode separation was $\sim 4\text{cm}$ and the pins were distributed over an area of $\sim 2 \times 100\text{ cm}^2$. The discharge was excited using an oil-immersed lumped-Blumlein inversion circuit, Fig 15, in which the capacitance could be readily varied, each stage consisting of up to 15 Sprague 40kV 2.4nF capacitors. Charging voltages from 20-40kV were used giving peak excitation fields up to 20kV cm^{-1} . Voltage and current waveforms were monitored using a capacitance divider probe and a fast current transformer respectively. The laser was operated using $\text{SF}_6\text{:H}_2$ mixtures at pressures up to ~ 100 torr; at pressures ≤ 40 torr the discharge appeared to be uniform whilst at higher pressures some localized arcs were observed superimposed on the uniform discharge. The occurrence of these arcs did not appear to significantly affect the characteristics of the laser output beam up to pressure ~ 100 torr.

2.3 Laser Performance

Operating Characteristics - Stable Resonator

A study of the laser performance was carried out using a stable resonator formed by a concave 10m radius of curvature Au coated copper alloy mirror and a plane NaCl etalon separated by 1.5m. The laser energy was measured using a Gentec pyro-electric joulemeter and the pulse shape monitored by scattering a small fraction of the output radiation onto a Judson InAs photovoltaic detector. The response time of the detector with 1 volt reverse bias was measured using a subnanosecond $1.06\mu\text{m}$ laser pulse to be $\sim 2\text{ns}$ risetime and $\sim 10\text{ns}$ falltime. This detector thus provided adequate time resolution for the experiments in which the laser pulse length was typically $\geq 100\text{ns}$.

In Fig 16 the variation of output energy with $\text{SF}_6 + \text{H}_2$ pressure ($P_{\text{H}_2}/P_{\text{SF}_6} = 1/9$, $V_c = 30\text{kV}$) shows a distinct maximum at $\sim 40\text{-}50$ torr. The variation with H_2 partial pressure is shown in Fig 17, the optimum H_2 pressure being in the range 4-8 torr for a fixed SF_6 partial pressure of 54 torr. Replacing the H_2 with C_3H_8 produced no significant change in the electrical or laser output characteristics with the exception of pulsewidth which was somewhat broader with C_3H_8 as the hydrogen donor. The output energy with C_3H_8 was found to optimise at ~ 40 torr total pressure with $P_{\text{C}_3\text{H}_8}/P_{\text{SF}_6} = 1/19$. When helium was added to $\text{SF}_6\text{-H}_2$ or $\text{SF}_6\text{-C}_3\text{H}_8$ mixtures the output energy was always reduced, the laser pulse shape remaining substantially unchanged.

In Fig 18, the variation of output energy with the lumped Blumlein charging voltage is shown for two values of the capacitor C_1 (Fig 15). Also shown is the variation when the Blumlein was replaced by a single $0.1\mu\text{F}$ capacitor.

The results shown in Figs 16-18 for $\text{SF}_6\text{-H}_2$ mixtures were obtained with $1\text{k}\Omega$ current limiting resistors; when 330Ω resistors were used there was no significant difference in the data. Since measurements of the laser current indicated that a relatively small fraction ($\sim 10\%$) of the discharge energy was dissipated in the ballast resistors the results would be expected to be approximately independent of the resistors used.

With an optimised $\text{SF}_6\text{-H}_2$ gas mixture of ~ 36 torr SF_6 , ~ 4 torr H_2 and 40kV charging voltage ($C_1 = 36\text{nF}$) the maximum laser output energy with the stable cavity was 1.1J , the peak power $\sim 4\text{MW}$ and the laser pulse shape as shown in Fig 19. The electrical-optical efficiency was 2%. With the stable resonator the beam divergence was measured to be $\sim 10\text{mrad}$ implying highly multi-mode oscillation. Since it is known that the gain of the HF laser can be very high⁽²⁶⁾ ($> 0.1\text{ cm}^{-1}$) this large divergence is probably due to parasitic modes superimposed upon the normal resonator modes. This is consistent with the finding that a substantial fraction of the laser energy appeared even with

the NaCl coupling mirror removed. Some reduction in the parasitic energy was achieved by coating the Brewster window mounts and the mirror holders with 'Nextal' matt black paint.

2.4 Unstable resonator studies

The high divergence of the pin laser when operated with a stable resonator precluded obtaining breakdown over the range of parameters of interest to this study. To improve the beam quality an unstable resonator configuration was therefore designed and fabricated, and tested under similar operating conditions to those described above. Previous studies with TEA CO₂ lasers⁽²⁷⁾ had shown that such resonators could lead to significant improvements in laser performance and were particularly suitable for high gain systems⁽²⁸⁾.

For the unstable resonator studies the cavity was formed by a 5cm diameter plane mirror and 1cm diameter, 9m radius of curvature convex mirror, both of which were Au-coated. The mirrors were separated by a distance of 1.5m and the convex output coupling mirror was mounted on a 2mm thick Infrasil flat. A 20° wedge angle between the Infrasil flat and the mirror surface was used to prevent feedback to the laser from the surfaces of the flat (Fig 20). From geometrical analysis^(29,4) the magnification, M , of the resonator was calculated to be 2.2, the round-trip loss factor, δ , 79% and the radius of curvature of the output annular wavefront at the convex mirror, R' , 5.5m. A variable diameter circular aperture placed in the cavity and located near the output coupling mirror was used to vary the outer diameter of the output beam. It should be noted that this aperture was used to control only the effective magnification, M_e , of the emerging annular beam, the cavity loss factor, δ , which is determined by the mirror parameters, remaining unchanged.

The far field of the unstable resonator output was formed by focusing with the mirror arrangement shown in Fig 20 and recorded by burning exposed Polaroid film. In preliminary experiments it was found that the full angular width of the focused spot was ~ 1 mrad showing a considerable improvement over results

with the stable resonator but still significantly larger than expected for diffraction limited performance. A detailed inspection of the far-field pattern indicated astigmatic wavefront aberration which was traced to the Brewster angle windows. This resulted from slight curvature (lensing) on the flats and was not due to the intrinsic aberration introduced by a tilted window into a diverging beam. To overcome the problem one of these windows was eliminated using an internal mirror cell and the other replaced by a high quality NaCl flat ($\sim \frac{1}{4} \lambda \text{ cm}^{-1}$ in the visible). The resulting far-field patterns were then found to be very close to diffraction limited; at M_e values ≤ 2.5 the far-field pattern exhibited a high degree of circular symmetry (Fig 21a); however, at larger apertures some degree of distortion was evident (Fig 21b). This distortion is attributed to residual wavefront aberrations introduced by the NaCl window and the Infrasil flat.

The radial energy distribution in the far-field ring pattern was obtained for various values of M_e by placing a circular aperture concentric with the pattern and measuring the transmitted energy as the aperture diameter was varied (Fig 20). Experimental results for $M_e = 1.5, 2.2$ and 3 are shown in Fig 22 together with the theoretical radial energy distributions for a uniformly illuminated annular aperture. The experimental results are seen to be in reasonably good agreement with the theoretical predictions.

The energy flux density distribution in the near field at distance $\sim 20\text{cm}$ from the output coupling mirror, was obtained on a shot by shot basis by scanning an apertured joulemeter (resolution 1mm) across the beam. Results of this measurement are shown in Fig 23 where it can be seen that the beam is considerably wider than expected from geometrical mode theory. The nonuniformity of the near field distribution (Fig 23) is probably sufficient to explain the discrepancies between the experimental and theoretical radial energy distributions in the far field shown in Fig 22.

The effectiveness of the unstable resonator in controlling parasitic oscillations was demonstrated using the experimental configuration shown in Fig 24.

With this arrangement any radiation falling outside the 2.0 mrad collection cone of the central hole in the plane mirror, M_2 , was reflected onto a joulemeter, E_2 (Fig 24). The central hole diameter was chosen to pass $> 95\%$ of the unstable resonator far-field energy for a diffraction limited beam with $M_e \geq 1.5$. The energy at E_2 and the total output energy, at E_1 , were then measured with and without the convex resonator mirror masked by a 1cm diameter absorbing black disc. With the disc in place the total 'parasitic' (i.e. no coupling mirror) energy was 0.32J and 72% of this energy was recorded at E_2 . With the unstable resonator operative, however, the fraction of energy at E_2 was drastically reduced being $\sim 2\%$ of the total output energy of 0.8J in this case. It thus appears from this experiment that the intracavity flux of the unstable resonator grows to a magnitude sufficient to cause gain saturation before the threshold for parasitic oscillation is reached. A similar effect has been reported for a dye laser operated with an unstable resonator⁽³⁰⁾.

The unstable resonator laser was also operated with $\text{SF}_6\text{-D}_2$ gas mixtures producing laser action at $\sim 3.6 - 4\mu\text{m}$ from DF. Again, careful studies of the beam quality using the system shown in Fig 20 showed that essentially diffraction limited performance was achieved as in the case of HF.

Parameter study for HF/DF operation

A parametric study of the unstable resonator laser was carried out for HF and DF operation in order to optimise the system performance. For these studies a fast, nitrogen cooled, Au doped Ge detector (SBRC) was used to obtain the laser pulse shape and energy measurements made using a commercial pyroelectric joulemeter. Peak power measurements were made by integrating the laser pulse shape and requiring that the area under the curve be equal to the laser energy; the accuracy of the power measurements was $\sim \pm 15\%$.

HF operation

In Fig 25 the dependence of laser energy and peak power on the relative concentration, γ , of hydrogen in the gas mixture is shown for various operating pressures and $V_C = 40\text{kV}$. Here $\gamma = P_H/(P_H + P_S)$ where P_H and P_S are the partial pressures of hydrogen and SF_6 respectively. Maximum energy and power output occur for $\gamma \approx 0.07$ and $\gamma \approx 0.15$ respectively, these optima being approximately independent of pressure over the range studied. The occurrence of significantly different optima for power and energy is attributed to the fact that maximum energy is obtained under conditions which maximise the net HF production during the excitation pulse⁽³¹⁾ whereas the highest peak power is expected to result when the initial rate of HF production is a maximum. Under the latter conditions the initial pump-rate and hence rate of rise of laser gain are optimised leading to high output power through efficient gain-switching in a similar manner to the TEA CO_2 laser⁽³²⁾. Qualitatively, the decrease in peak power for non-optimum γ can be explained by noting that for low γ there is insufficient H_2 for rapid HF production via the reaction $\text{H}_2 + \text{F} \rightarrow \text{HF} + \text{H}$, whereas for high γ the F atom concentration is reduced due to decreased SF_6 dissociation. The latter is a result of the increased discharge energy losses due to ionization and dissociation of H_2 ⁽³¹⁾. For optimum energy output the HF production rate must be maximised consistent however with minimising the deactivation of vibrationally excited HF; the optimum γ for energy thus occurs at lower values than for power, since although the HF production rate decreases, vibrational relaxation of HF by H_2 and H ⁽³¹⁾ is reduced leading to longer duration pulses. This is supported by the experimental results which show that the laser pulse width increases progressively with decreasing γ , varying from $\sim 160\text{ns}$ at $\gamma = 0.36$ to $\sim 2\mu\text{s}$ at $\gamma = 0.01$.

The variation of laser energy and power with the total mixture pressure is shown in Fig 26, for an $\text{SF}_6\text{-H}_2$ mixture ratio optimised for energy ($\text{SF}_6/\text{H}_2 \sim 13/1$) and charging voltages of 40 and 25kV. The pressure at which the energy output

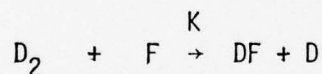
maximises with $V_C = 40\text{kV}$ is ~ 44 torr, the output under these conditions being $\sim 650\text{mJ}$. At $V_C = 25\text{kV}$ the energy maximises at a lower pressure of 30 torr giving energies of $\sim 300\text{mJ}$. In both cases it can be seen from Fig 26 that maximum peak power is obtained at a considerably higher pressure than those corresponding to the optimum energy. It is again possible to interpret this result in terms of the different conditions that must be satisfied for efficient energy extraction and efficient gain-switching as discussed previously. At high pressures the pumping reaction $\text{H}_2 + \text{F} \rightarrow \text{HF} + \text{H}$ proceeds more rapidly leading to efficient gain-switching and the generation of high peak powers but the laser pulse width (and hence energy) is reduced due to increased vibrational deactivation. For the conditions of Fig 26 and $V_C = 40\text{kV}$, the pulse width decreased from $\sim 1\mu\text{s}$ to $0.4\mu\text{s}$, as the pressure was increased from 15 torr to 90 torr. For the same pressure range and $V_C = 25\text{kV}$, the pulse width varied from $1.5\mu\text{s}$ to $0.3\mu\text{s}$.

From the time resolved measurements of the discharge voltage it was found that with the optimum operating conditions for energy extraction of $V_C = 40\text{kV}$ and $p = 44$ torr, the average excitation field sustained on the laser discharge channel was $\sim 260 \text{ Vcm}^{-1} \text{ torr}^{-1}$ which corresponds to an average discharge electron energy of $\sim 3\text{eV}$. This result is in agreement with measurements reported by Obara and Fujioka⁽³³⁾ who show that for a given excitation voltage the optimum pressure is that at which the average discharge electron energy matches the dissociation energy of SF_6 which is $\sim 3.1\text{eV}$. Thus, as the excitation voltage is decreased the optimum pressure decreases⁽³³⁾ (Fig 26) since this maintains the appropriate average electron energy for efficient SF_6 dissociation. Measurements made of the influence of charging voltage on laser performance with otherwise fixed parameters, showed the power and energy to be linearly dependent upon V_C between 20 and 40kV. For an optimised gas mixture, maximum laser efficiency of $\sim 1.1\%$ was obtained at a charging voltage of 30kV.

DF operation

A study of the laser performance for DF operation was made in order to provide comparative data for the HF laser studies and also to define suitable operating conditions for use of the laser in breakdown studies.

In Fig 27 the variation of DF laser energy at peak power is shown as a function of γ for $V_C = 40\text{kV}$ and pressures of 22 torr and 37.6 torr. Here γ is defined as $P_D / (P_D + P_S)$ where P_D is the partial pressure of deuterium and P_S the partial pressure of SF_6 in the gas mixture. As with the HF laser the optimum γ for energy output is lower than that for peak power, the optimum lying at $\gamma \approx 0.1$ and $\gamma \approx 0.2$ respectively (Fig 27). These values are slightly higher than those obtained for the HF laser. Under comparable conditions the DF laser pulse length was found to be longer than that for HF operation, the pulse width varying from $\sim 3.0\mu\text{s}$ at $\gamma \approx 0.022$ to $0.170\mu\text{s}$ at $\gamma \approx 0.39$. The increased pulse width with DF is attributed to the fact that the rate constant K for the formation of DF via the reaction



is smaller than the corresponding reaction for HF by a factor of $\sim 1.3^{(34)}$. This limits the DF production rate and maximum laser energy extraction rate to lower values than for HF.

The variation of DF laser energy and peak power with pressure for an energy optimised mixture ($\text{SF}_6/\text{D}_2 = 9/1$) is shown in Fig 28 for $V_C = 40\text{kV}$ and 25kV . A maximum output energy of $\sim 600\text{mJ}$ was obtained at 50 torr total pressure with $V_C = 40\text{kV}$. As with the HF laser the optimum pressure for energy extraction decreased as the excitation voltage was reduced (Fig 28).

HF and DF Emission Spectra

A study was made of the multiline emission spectrum of the HF/DF laser when operated using $\text{SF}_6\text{-H}_2$ and $\text{SF}_6\text{-D}_2$ gas mixtures. The output laser radiation was focused into a 0.8 metre Czerny-Turner monochromator which was equipped with 300 $\text{\AA}/\text{mm}$ and 250 $\text{\AA}/\text{mm}$ blazed diffraction gratings for HF and DF measurements respectively. For spectral energy distribution measurements this detector was replaced by a pyroelectric joulemeter.

For an energy optimised mixture of $\text{SF}_6/\text{H}_2 \sim 13/1$ and $p \approx 45$ torr the HF laser emission spectra was observed to consist of 18 P branch transitions in the $3 \rightarrow 2$, $2 \rightarrow 1$ and $1 \rightarrow 0$ vibrational bands of HF. The emission spectrum covered the wavelength range $2.6 - 3.0 \mu\text{m}$, the distribution of energy in the various lines being as shown in Fig 29. Maximum energy was obtained in the $P_{2 \rightarrow 1}$ band, the $P_{1 \rightarrow 0}$ having a similar but slightly lower energy content. The relative distribution of energy in the $P_{3 \rightarrow 2} : P_{2 \rightarrow 1} : P_{1 \rightarrow 0}$ bands was $0.88 : 1 : 0.26$ which can be compared with a calculated distribution of $0.84 : 1 : 0.25$ reported by Hough and Kerber⁽³⁵⁾ for the $\text{SF}_6\text{-H}_2$ chemical laser.

From time resolved measurements it was found that the P(3), P(4) and P(5) lines in the $2 \rightarrow 1$ band oscillated first, these lines being delayed by $\sim 70\text{ns}$ with respect to the start of the current pulse. The observation of earliest lasing on the $P_{2 \rightarrow 1}$ band is consistent with the fact that the pumping reaction $\text{H}_2 + \text{F} \rightarrow \text{HF} + \text{H}$ selectively populated the $V = 2$ level of HF⁽³⁴⁾. Simultaneous lasing on several J lines of a given vibrational band was observed to occur, giving evidence of relatively slow rotational relaxation at the pressures employed⁽³⁵⁾. Sequential J shifting from low to high values also occurred through the laser pulse as reported by previous investigators⁽³⁶⁾. This behaviour may result due to a decrease in vibrational temperature which occurs as laser energy is extracted or through an increase in rotational temperature during the laser pulse, or, possibly, due to a combination of these effects.

For $\text{SF}_6\text{-D}_2$ operation, the laser emission spectrum consisted of 26 P branch lines in the $4 \rightarrow 3$, $3 \rightarrow 2$, $2 \rightarrow 1$, $1 \rightarrow 0$ vibrational bands of DF. The distribution of energy in

the lines is shown in Fig 30 for an energy optimised mixture ratio of $\text{SF}_6\text{-D}_2$ 9/1; the relative energy per band was $P_{4\rightarrow3} : P_{3\rightarrow2} : P_{2\rightarrow1} : P_{1\rightarrow0} = 0.12; 0.82; 1; 0.71$. Earliest lasing occurred on the 3 \rightarrow 2 band ($P_{3\rightarrow2}(4)$) with a delay of ~ 100 ns with respect to the start of the current pulse. Simultaneous lasing within a given band and sequential J shifting was observed as with HF operation.

2.5 HF/DF Breakdown measurements

The experimental arrangement used to measure thresholds is shown in Fig 31. The output from the unstable resonator was directed by mirror M_1 into a pressure cell, C, which could be either evacuated ($p \ll 1$ torr) or pressurised to ~ 10 atm (Fig 31). Radiation entered the cell through a tilted NaCl window and was brought to a focus by a 25cm focal length mirror, M_3 , at an effective aperture ratio of ≥ 6.5 . An NaCl beam splitter, B, was used to direct a known fraction of the incident laser radiation onto a calibrated joulemeter (Lumonics 20D) to monitor the laser energy on each shot. Scattered laser radiation from the joulemeter surface was detected by a high speed Au doped Ge detector, D, terminated in 50Ω and the pulse shape displayed on a Tektronix 556 oscilloscope. For measurements with the HF laser a set of attenuators, A, (Fig 31) was constructed using Infrasil substrates coated with thin films of Inconel to provide an approximately wavelength independent attenuation over the laser emission spectrum. Robust and damage resistant coatings were obtained by depositing the Inconel film on heated substrates ($\sim 200^\circ\text{C}$). For the DF laser, glass filters were used as attenuators (Chance-Pilkington, Type ON).

Particular care was taken in the experiments to preserve the high beam quality furnished by the unstable resonator. For example, provision was made to monitor the far-field distribution during a series of breakdown measurements by removing the kinematically located turning mirror M_1 (Fig 31); in this way any misalignment of the resonator could be easily observed and corrected. The

breakdown cell was carefully aligned with respect to the incident laser beam to minimise off-axis aberrations and the optical components used in the system were tested by observing their effect on the far-field distribution and were chosen to give negligible beam degradation.

It is interesting to note that gas breakdown could be obtained in the cell at relatively low pressures (< 1 atmosphere in air) even when the output coupling mirror of the unstable resonator was removed. This is thought to be because the remaining laser mirror and breakdown mirror formed a high loss unstable resonator with an intracavity focus. With the output coupling mirror in place, however, the attainment of breakdown was always found to be critically dependent upon the resonator alignment indicating that, under these conditions, the laser was controlled by the primary unstable resonator.

In our experiments the breakdown threshold was defined as the intensity, ϕ_T , at which the probability for spark formation was 0.5, where ϕ_T is given by

$$\phi_T = \frac{4\beta P_0}{\pi d_0^2}$$

Here P_0 is the threshold laser power determined from the measured laser energy and pulse shape, β is the fraction of energy in the central lobe of the far field diffraction pattern (typically $\sim 60\%$ in these experiments) and d_0 is the diameter of the first minimum of the diffraction pattern which is derived from the measured diffraction angle (Fig 22) and the mirror focal distance. ϕ_T is thus an average intensity over the central lobe and may underestimate the breakdown intensity since the peak on-axis intensity is computed to be ~ 4 times higher for a diffraction limited profile. We chose to use ϕ_T , however, since it could be derived from directly measured quantities. For the HF laser the spot size, d_0 , was calculated to be $\sim 40\mu\text{m}$. An estimate of the blur diameter, δ , introduced by spherical aberration can be made using⁽³⁷⁾

$$\delta \approx \frac{8 \times 10^{-3}}{F^3} f$$

where F is the effective aperture ratio of the focusing mirror and f the focal distance. For $F \geq 6.5$ and $f = 26\text{cm}$, δ is calculated to be $\leq 8\mu\text{m}$ and, assuming the spot diameters combine as⁽³⁸⁾ $(d_0^2 + \delta^2)^{1/2}$, spherical aberration can be neglected in calculating the spot size. The HF laser pulse duration was $\sim 120\text{ ns}$ at fwhm (Fig 32a) and although there was some structure this was reproducible. For DF the spot size was calculated to be $\sim 50\mu\text{m}$. The DF laser pulse shape (Fig 32b) also had a reproducible structure, the effective pulsewidth at fwhm being similar to that for HF. In these experiments the relative error in the threshold determination was estimated to be $\pm 20\%$ and the absolute error approximately $\pm 50\%$.

Experimental Results and Discussions

Figs 33-35 show experimentally determined breakdown thresholds, ϕ_T , for multiline HF laser radiation focused in various gases. In Fig 33, the variation of ϕ_T with pressure over the range $\sim 300\text{-}3400\text{ torr}$ is shown for dry air together with some data for laboratory air. It is evident that there is no significant difference in the two cases. At a pressure of 760 torr a breakdown threshold of $\sim 6.10^{10}\text{ W.cm}^{-2}$ was found and, assuming a single power law dependence upon pressure, p , a least squares fit to the data gave $\phi_T \sim p^{-0.6}$. Data were also obtained using research grade N_2 and, as can be seen from Fig 34, the threshold value and pressure scaling are very similar to those determined for air. This result suggests that the N_2 component in air is dominant in the breakdown process, presumably because of the strong inelastic energy losses associated with vibrational excitation in this gas⁽¹³⁾. The measured pressure dependence ($\phi_T \sim p^{-0.6}$) is very similar to that reported for N_2 breakdown with CO_2 laser radiation at pressures less than $\sim 3000\text{ torr}$ ^(13,39).

In Fig 35 similar data are shown for breakdown in ultra-pure Ar. The threshold at atmospheric pressure was determined to be $1.6 \times 10^{10}\text{ W.cm}^{-2}$ which is approximately four times lower than for air, and a pressure scaling $\phi_T \sim p^{-0.95}$ was deduced from the data. This latter result, whilst agreeing

with low pressure breakdown data at other wavelengths^(39,11), is surprising, since for the spot size employed in our experiments, diffusion losses are calculated to be important at low pressures giving a theoretical pressure dependence of $\phi_T \sim p^{-2}$ (11). Such calculations assume, however, free electron diffusion which may seriously overestimate the losses during the latter stages of breakdown phase when the electron density exceeds $\sim 10^8 \text{ cm}^{-3}$ and ambipolar diffusion is expected to become important. It is also probable that losses due to excited state production⁽¹²⁾ and recombination⁽¹¹⁾ will significantly modify the pressure scaling.

Breakdown thresholds were also determined for multiline DF laser radiation focused in dry air and the results of the variation of ϕ_T with pressure over the range $\sim 150 - 3600$ torr are shown in Fig 36. The pressure scaling for $p \geq 300$ torr is similar to that obtained for HF laser radiation (Fig 33) but, as expected for the longer wavelength radiation, the threshold is significantly lower. For cascade ionization, theory predicts a threshold scaling with wavelength, λ , of $\phi_T \sim \lambda^{-2}$ which gives a ratio of 1.84 for the HF and DF thresholds assuming $\lambda = 2.8\mu\text{m}$ and $3.8\mu\text{m}$ respectively. Experimentally the ratio at atmospheric pressure is ~ 2 which is in good agreement with cascade theory considering the multiline nature of the radiation.

In our studies no effort was made to filter the gases entering the cell but analysis of the particle size distribution down to particle sizes of $1\mu\text{m}$ (Royco Particle Counter Model 245) was possible and showed that the concentration of these and larger particles was not sufficient to significantly affect the breakdown threshold⁽⁴⁰⁾ for the focal spot dimensions employed. In this respect the measured values of ϕ_T are effectively those of 'clean' air⁽⁴¹⁾.

It was found that breakdown could be obtained reliably throughout these experiments with no auxiliary ionization and it is likely that initial electrons arise from the irradiation of submicron particles within the focal volume. It is also possible that initial electrons are produced by laser induced dissociation

of absorbing gases (present as trace impurities) as has been suggested by Isenor and Richardson⁽⁴²⁾ for CO₂ laser produced gas breakdown. Some preliminary experiments in our laboratory in which HF laser radiation is focused into absorbing gases show that sub-threshold luminescence can occur and that in these gases the breakdown threshold is considerably lower than for non-absorbing gases.

To make a direct comparison of these data with measurements at other infrared wavelengths, care must be taken to ensure that similar experimental conditions were used since the absolute threshold value is sensitive to many parameters such as spot size and intensity distribution, pulse length and particulate contamination. However, using atmospheric pressure clean air threshold data at 1.06 μ m⁽⁴¹⁾ and 10.6 μ m⁽⁴⁰⁾ for comparable pulse lengths and spot sizes we obtain good agreement with a λ^{-2} wavelength scaling for the peak on-axis breakdown intensity.

Figure Captions

- Fig 1 TEA CO₂ laser system.
- Fig 2 Input energy flux density versus output energy flux density for nanosecond pulses (Gain = 10^4).
- Fig 3 Polariser analyser configuration
(a) GaAs switch activated
(b) Loss of amplified spontaneous emission from system in the unswitched state
- Fig 4 Mode locked unstable resonator oscillator
- Fig 5 (a) Amplified laser pulse monitored on a photon drag detector and displayed on a Tektronix 7904 oscilloscope
(b) Ion time of flight signals (probe separation 50cm)
(c) X-ray detector signals.
- Fig 6 Asymptotic ion expansion velocity versus flux density for irradiation of carbon target with 5ns pulse (spot size 140 μ m).
- Fig 7 CO₂ laser pulse shape used in gas breakdown measurements.
- Fig 8 Pulse width dependence of breakdown in Argon at various pressures ($\lambda = 10.6\mu$ m)
- Fig 9 Pressure dependence of Argon breakdown threshold for various pulse widths ($\lambda = 10.6\mu$ m).

- Fig 10 Breakdown threshold versus pressure x pulse length ($\lambda = 10.6\mu\text{m}$)
- Fig 11 Breakdown threshold of N_2 versus pulse width ($\lambda = 10.6\mu\text{m}$)
- Fig 12 Breakdown threshold of N_2 versus pressure ($\lambda = 10.6\mu\text{m}$)
- Fig 13 Experimental circuit for resistive electrode studies.
- Fig 14 Circuit for u.v. pre-ionizer experiments.
- Fig 15 HF Pin laser, showing lumped Blumlein circuit configuration.
- Fig 16 Laser energy versus $\text{SF}_6 + \text{H}_2$ total pressure ($V_c = 30\text{kV}$ and $P_{\text{H}_2}/P_{\text{SF}_6} = 1/9$).
- Fig 17 Laser energy versus H_2 partial pressure ($P_{\text{SF}_6} = 54$ torr, $V_c = 30\text{kV}$)
- Fig 18 Laser energy versus charging voltage for three circuit configurations;
curve A Blumlein $C_1 = 15 \times 2.4\text{nF}$
curve B Blumlein $C_1 = 10 \times 2.4\text{nF}$
- Fig 19 HF laser pulse shape
- Fig 20 Unstable resonator configuration and mirror arrangement for studying far field. M_1 - plane, M_2 - 9m radius of curvature convex, M_3 - 10m radius concave, M_4 - 20m radius of curvature concave, A_1, A_2 - variable apertures (A_2 located in focal plane of mirror system), E - joulemeter.
- Fig 21 Far field burn pattern recorded on exposed Polaroid film
(a) $M_e = 1.5$ (b) $M_e = 3$

Fig 22 Calculated and experimental radial energy distribution in the far field - calculated for uniformly illuminated aperture ($\lambda = 2.7\mu\text{m}$) with various values for the magnification M (inner diameter of constant)

Exp. data ▽ $M_e = 1.5$

● $M_e = 2.2$

■ $M_e = 3$

Fig 23 Energy flux density distribution in the near field with aperture A , fully open.

Fig 24 Experimental configuration for studying the control of parasitic oscillation. M_1 - 10cm diameter, 2m radius of curvature - concave, M_2 plane with 2mm diameter 45° hole, E_1, E_2 - joulemeter locations.

Fig 25 Variation of (a) HF laser energy and (b) HF laser power with γ ($P_H/(P_H + P_S)$) for various pressures.

Fig 26 Variation of HF laser energy and power with total operating pressure.

Fig 27 Variation of DF laser energy and power with γ ($P_D/P_D + P_S$) for various pressures.

Fig 28 Variation of DF laser energy and power with total operating pressure.

Fig 29 Relative emission line energy distribution for HF operation.

Fig 30 Relative emission line energy distribution for DF operation.

Fig 31 Experimental configuration for breakdown studies. A - attenuator stack; M_1 - removable plane mirror, M_2 - 2m mirror; M_3 - focusing mirror; B - NaCl beam splitter; C - pressure cell; D - pulse-shape monitor; E - joulemeter.

Fig 32 Typical laser pulse shapes for HF/DF laser breakdown measurements.

Fig 33 HF laser breakdown threshold ϕ_T versus pressure for laboratory air (Δ) and dry bottled air (O).

Fig 34 HF laser breakdown threshold ϕ_T versus pressure for N_2

Fig 35 HF laser breakdown threshold ϕ_T versus pressure for Ar

Fig 36 DF laser breakdown threshold ϕ_T versus pressure for dry bottled air.

References

1. G.A. Hill, D.J. James and S.A. Ramsden, Opt. Commun. 9, 237, 1973.
2. P.E. Dyer, D.J. James and S.A. Ramsden, J. Appl. Phys. 44, 2408, 1973.
3. L.M. Frantz and J.S. Nodvik, J. Appl. Phys. 34, 2346, 1963.
4. P.E. Dyer and D.J. James, Appl.Phys.Lett., 26, 331, 1975.
5. P.E. Dyer, D.J. James, S.A. Ramsden and M.A. Skipper, Phys. Lett., 48A, 311, 1974.
6. P.E. Dyer, D.J. James, S.A. Ramsden and M.A. Skipper, Appl.Phys.Lett., 24, 316, 1974.
7. P.E. Dyer, D.J. James, G.J. Pert, S.A. Ramsden and M.A. Skipper, "Laser Interaction and Related Plasma Phenomena", Vol.3, ed. H. Schwarz and H. Hora, Plenum N.Y., 1974.
8. F.C. Jahoda, E.M. Little, W.E. Quinn, G.A. Sawyer and T.F. Stratton, Phys.Rev. 119, 843, 1960.
9. A.W. Ehler, paper presented at VIIIth Int. Quant. Elect. Conf., San Francisco, 1974.
10. D.C. Smith, Appl.Phys.Lett., 19, 405, 1971.
11. F. Morgan, L.R. Evans and C. Grey Morgan, J.Phys.D: Appl.Phys. 4, 225, 1971.
12. S.D. Rockwood, IEEE J. Quantum Electr., QE-10, 732, 1974.
13. M.P. Hacker, D.R. Cohn and R.L. Brooks, Appl.Phys.Lett., 24, 173, 1974.
14. P.J. Berger and D.C. Smith, Appl.Phys.Lett., 21, 167, 1972.
15. Y.L. Pan, R. Simpson, A.F. Bernhardt, Appl.Phys.Lett., 24, 87, 1974.
16. S.D. Rockwood, G.H. Canavan and W.A. Proctor, IEEE. J. Quantum Electr., QE-9, 154, 1973.
S.D. Rockwood, G.H. Canavan and W.A. Proctor, IEEE J. Quantum Electr. (Corresp.), QE-9, 782, 1973.

17. H. Pummer, W. Breittfeld, H. Wedler, G. Klement and K.L. Kompa, Appl.Phys. Lett., 22, 319-320, 1973.
18. R.G. Wenzel and G.P. Arnold, IEEE J. Quantum Electr., QE-8, 26-27, 1972.
19. F. Voignier and M. Gastaud, Appl.Phys.Lett. 25, 649-650.
20. A. Jay Palmer, Appl. Phys. Lett., 25, 138-140, 1974.
21. S. Solimeno, L. Nicolais, and F. Beretta, Ist Int. Conf. on Electrode Phenomena in Gas Discharges, Bucharest, 1974.
22. L. Nicolais, S. Solimeno and L. Nicodemo (to be published).
23. B.L. Tait and G. Salvetti, Department of Applied Physics Report, Hull, 1975.
24. H.J.J. Seguin, J. Tulip and D. McKen, Appl. Phys. Lett., 23, 344-346, 1973.
25. L.G. Christophorou, D.L. McCorkle and J.G. Carter, Journal of Chemical Physics, 54, 253-260, 1971.
26. C.R. Jones, Appl. Phys. Lett. 22, 653-655, 1973.
27. P.E. Dyer, D.J. James and S.A. Ramsden, Optics Commun., 5, 236-238, 1972.
28. K.I. Zemskov, A.A. Isaev, M.A. Kazaryan, G.G. Petrash and S.G. Rautain, Sov. J. Quant. Electron., 4, 474-477, 1974.
29. A.E. Seigman, Proc. IEEE, 53, 277, 1965.
30. T.F. Ewanizky, Appl. Phys. Lett., 25, 295, 1974.
31. J.L. Lyman, Appl. Optics, 12, 2736, 1973.
32. K.J. Andrews, P.E. Dyer and D.J. James, J.Phys.E., 8, 493, 1975.
33. M. Obara and T. Fujioka, Jap. J. Appl. Phys., 13, 995, 1974.
34. K.L. Kompa, Chemical Lasers, Topics in Current Chemistry, Springer Verlag, New York, 1973.

35. J.J.T. Hough and R.L. Kerber, Appl. Optics, 14, 2960, 1975.
36. J.V. Parker and R.R. Stephens, Appl. Phys. Lett., 22, 450, 1973.
37. W.J. Smith, Modern Opt. Engineering (McGraw Hill), New York 1966.
38. W.L. Smith, J.H. Bechtel and N. Bloembergen, Phys. Rev., B12, 706, 1975.
39. G.A. Hill, D.J. James and S.A. Ramsden, J.Phys.D., Appl.Phys. 5, L97, 1972.
40. D. Lencioni, Appl. Phys. Lett., 23, 12, 1973.
41. D. Lencioni, Appl. Phys. Lett., 25, 15, 1974.
42. N. Isenor and M.C. Richardson, Appl.Phys.Lett., 18, 224, 1971.

Publications

P.E. Dyer, D.J. James, S.A. Ramsden and M.A. Skipper, Phys. Lett. 48A, 311, 1974.

P.E. Dyer, D.J. James, S.A. Ramsden and M.A. Skipper, Appl.Phys.Lett. 24, 316, 1974.

P.E. Dyer, D.J. James, G.J. Pert, S.A. Ramsden and M.A. Skipper, Laser Interaction and Related Plasma Phenomena, Vol.3, ed. H. Schwarz and H. Hora, Plenum Press, N.Y. 1974.

B.K. Deka, P.E. Dyer and D.J. James, Optics Commun. 18, 462, 1976.

B.K. Deka, P.E. Dyer, D.J. James and S.A. Ramsden, Optics Commun. 19, 292, 1976.

RESISTIVE ELECTRODE SYSTEMS

Resistive electrode type	Resistivity Ω cm	C	V (kV)	C _p	Gap	Input energy J/l
1. SAN + graphite/ circular/5cm diameter, 4mm thick	200	2.5 μ F	35-40	—	~3.5cm	60-70
2.(a) SAN + 98-99% graphite powder/ 10cm x 20cm x 2 cm	200	0.02 μ F	20	—	~3.5cm	25
(b) " "	"	"	32	250pf	"	≥50
(c) " "	"	0.01 μ F	25	—	"	35
(d) " " with profile	"	0.02 μ F	20	—	"	30
3. SAN + Nat. graphite powder/10cm x 20cm x 2cm	400	0.02 μ F	20	—	"	20

Typical Gas Mixture

160 torr He, 35-40 torr SF₆ and 5 torr H₂

TABLE I

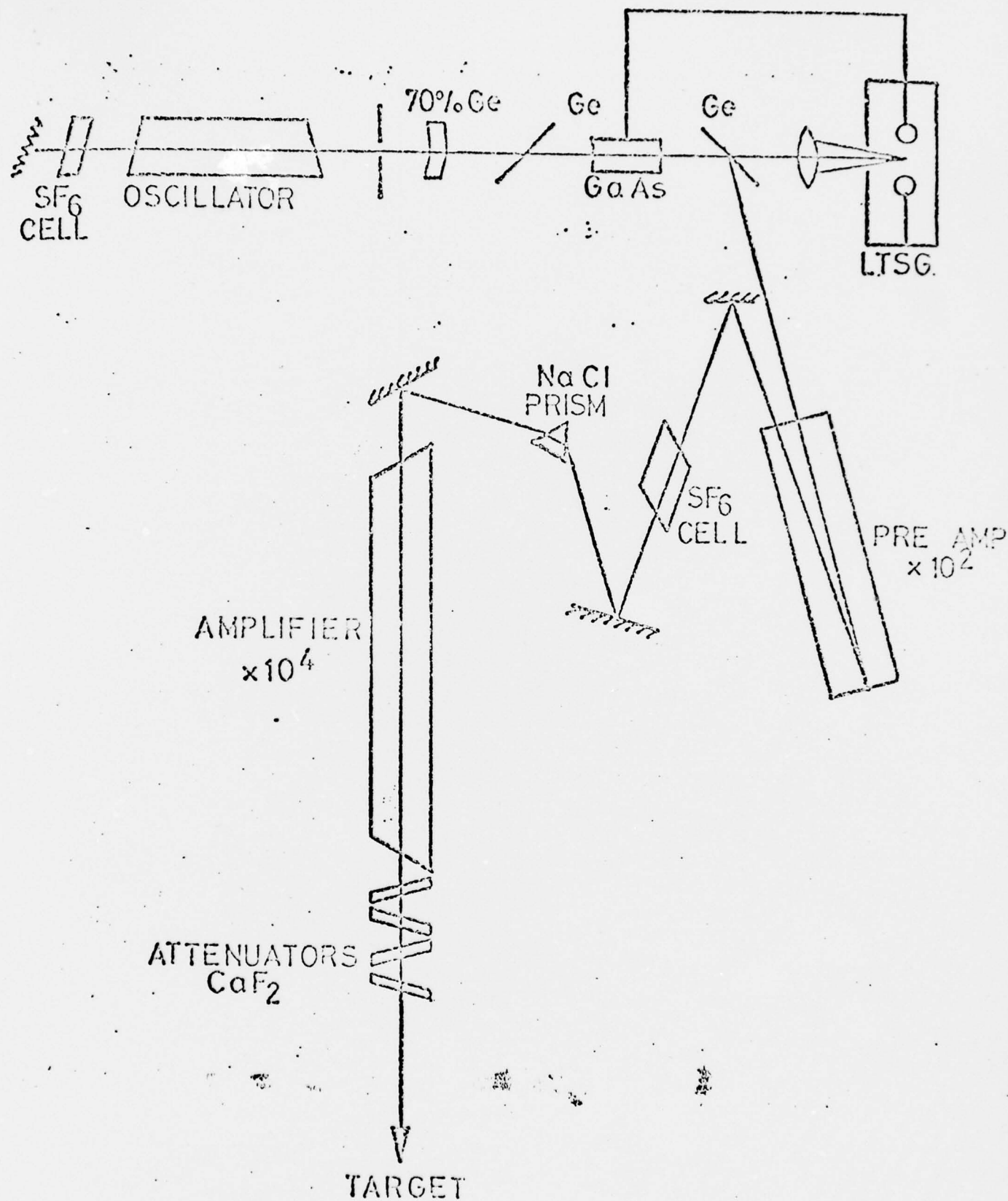


Fig. 1. TEA. CO₂ LASER SYSTEM

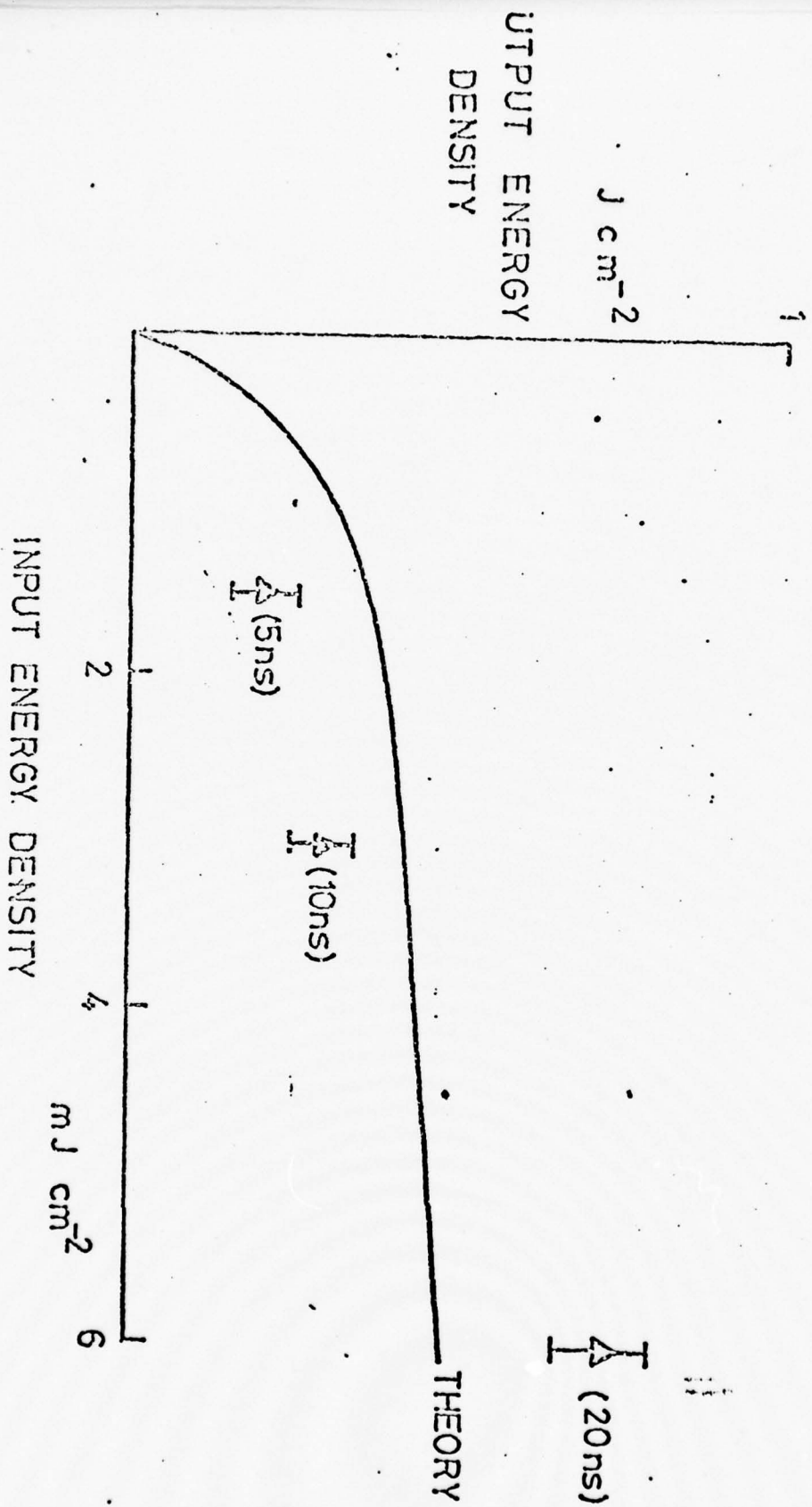


Fig 2

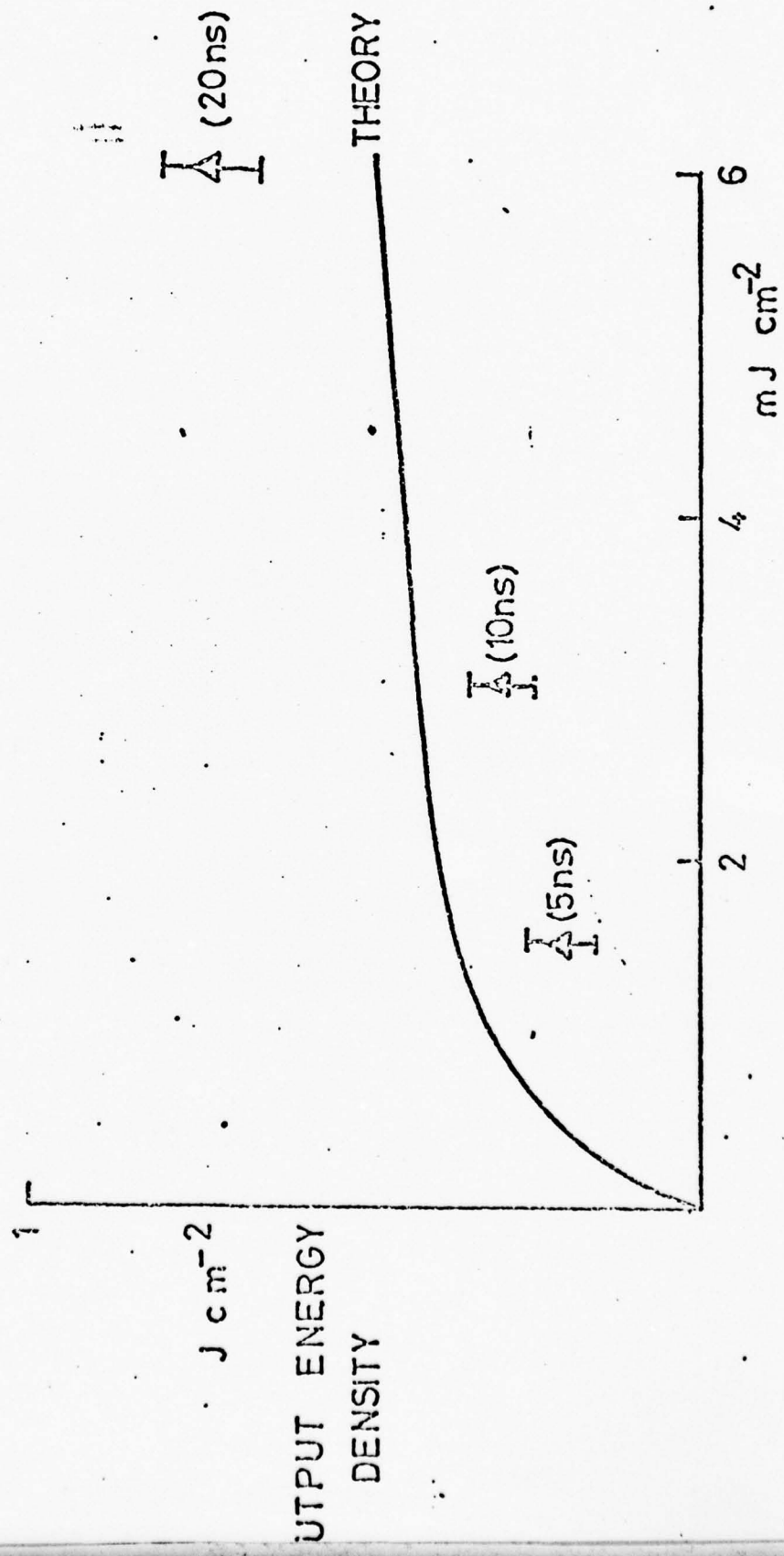


Fig 2

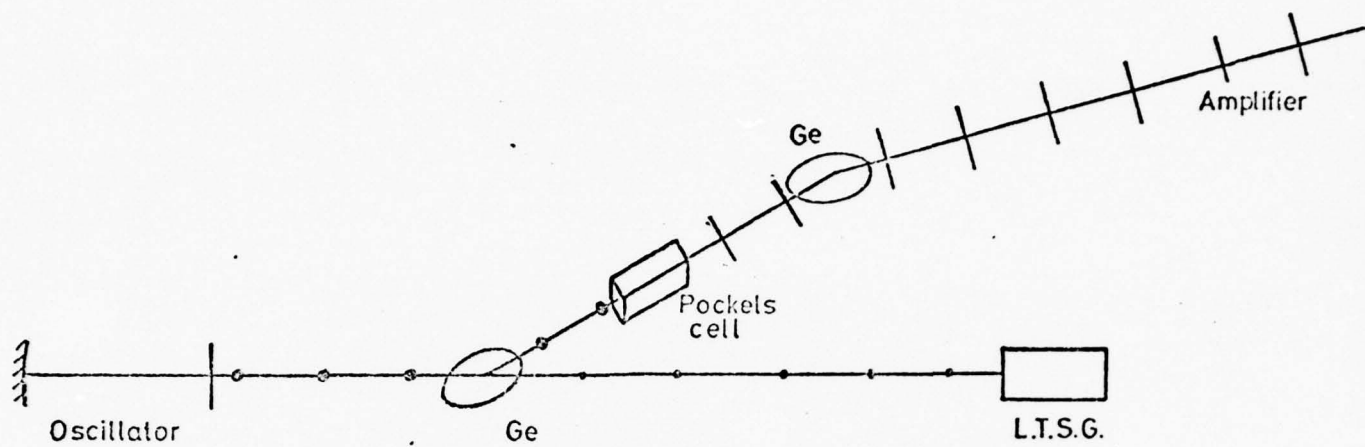


Fig 3(a)

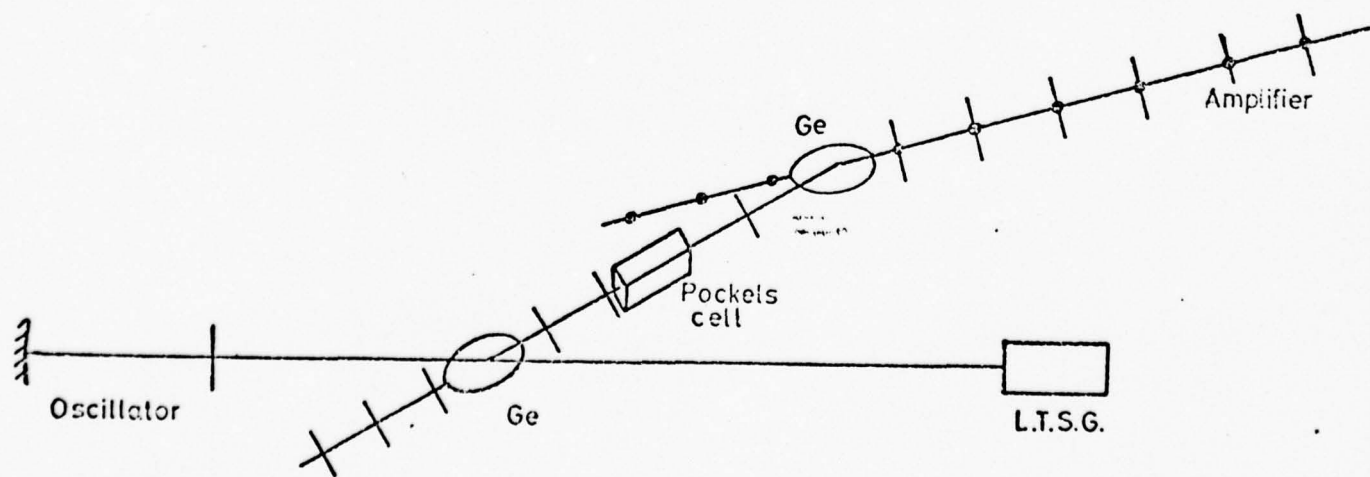


Fig 3(b)

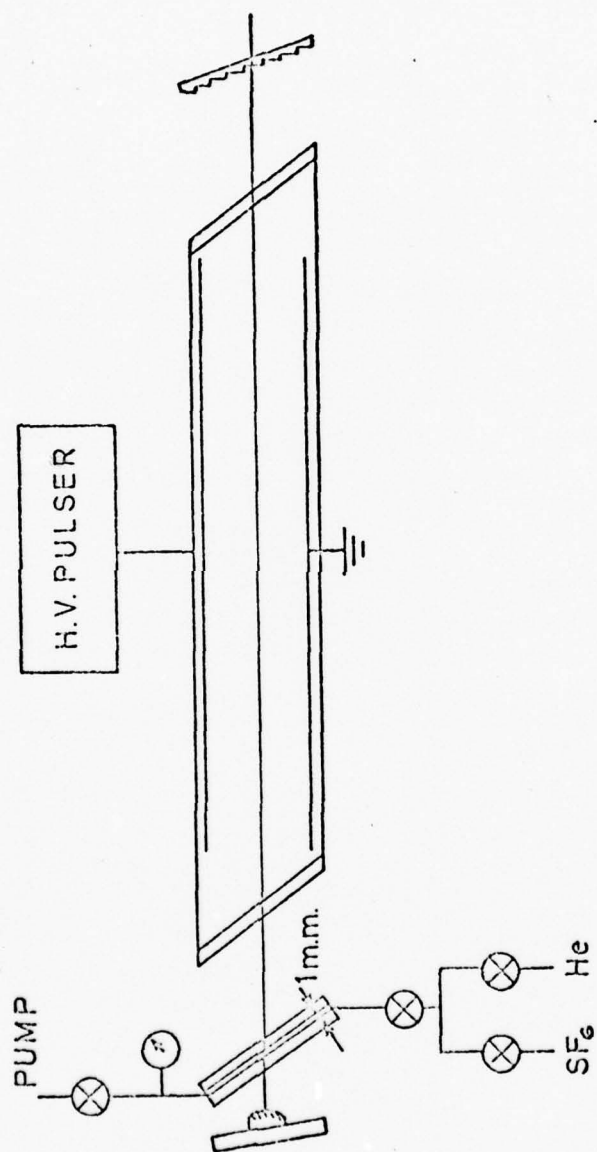


Fig 4

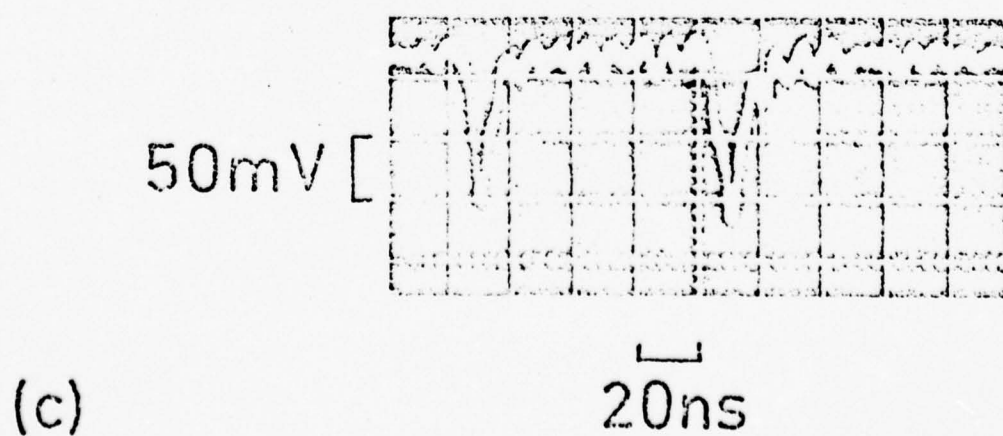
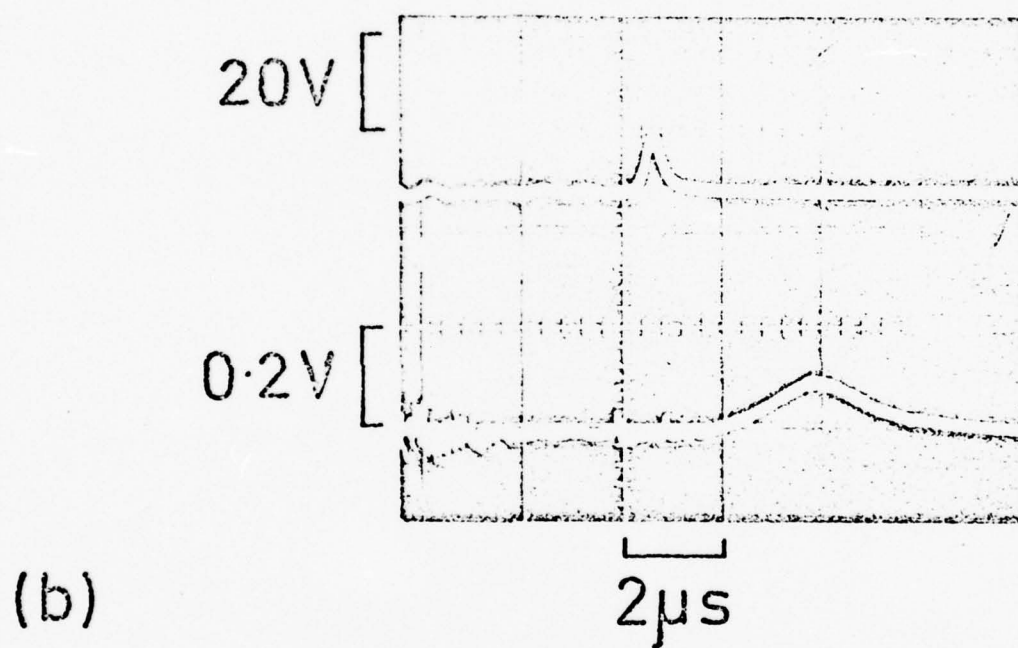
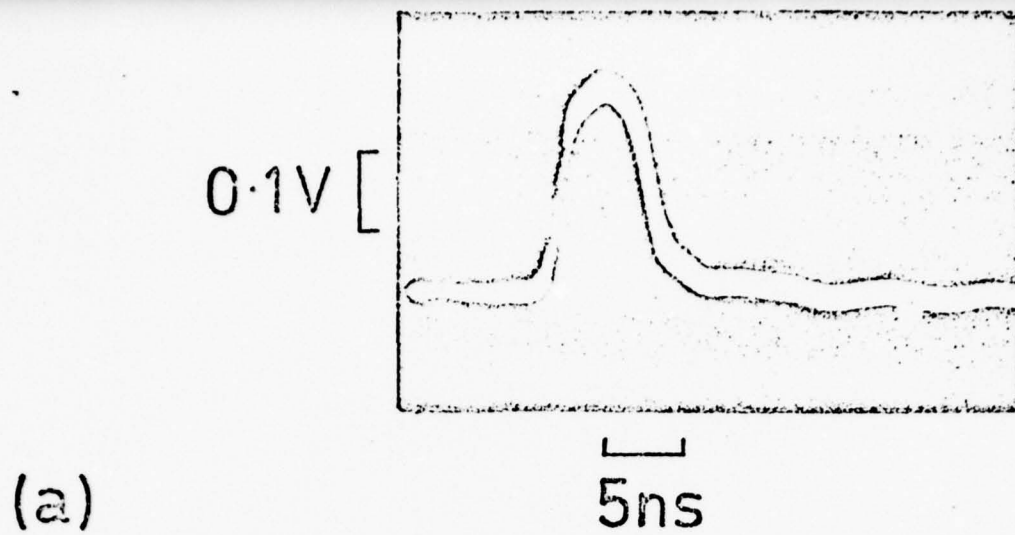


Fig 5

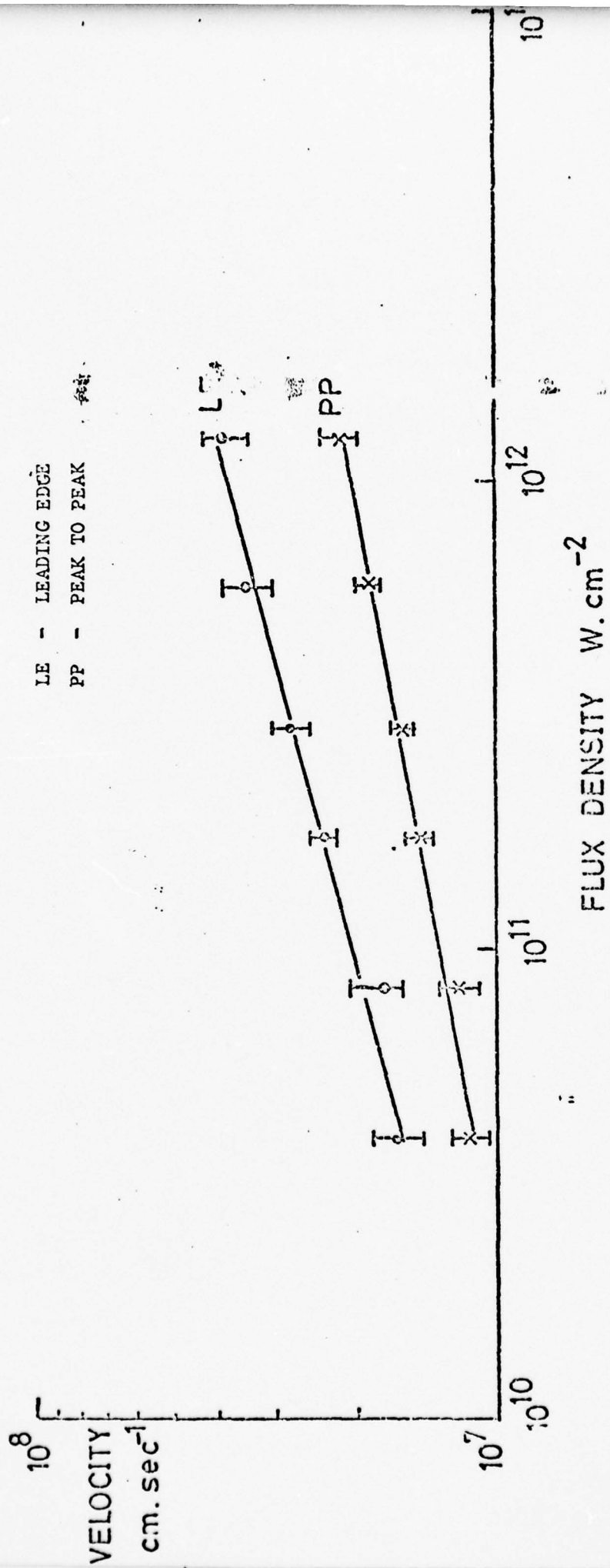
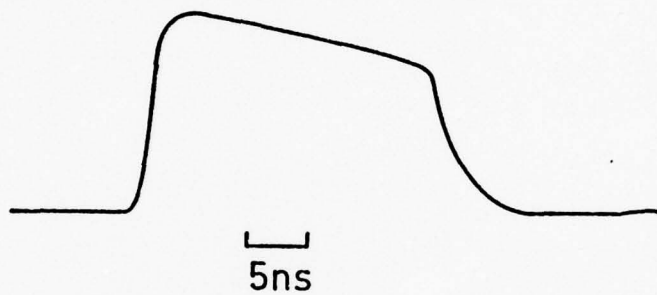


FIG 6



Single axial mode amplified T.E.A. CO₂
laser pulse, 5nsec. div.¹

Fig 7

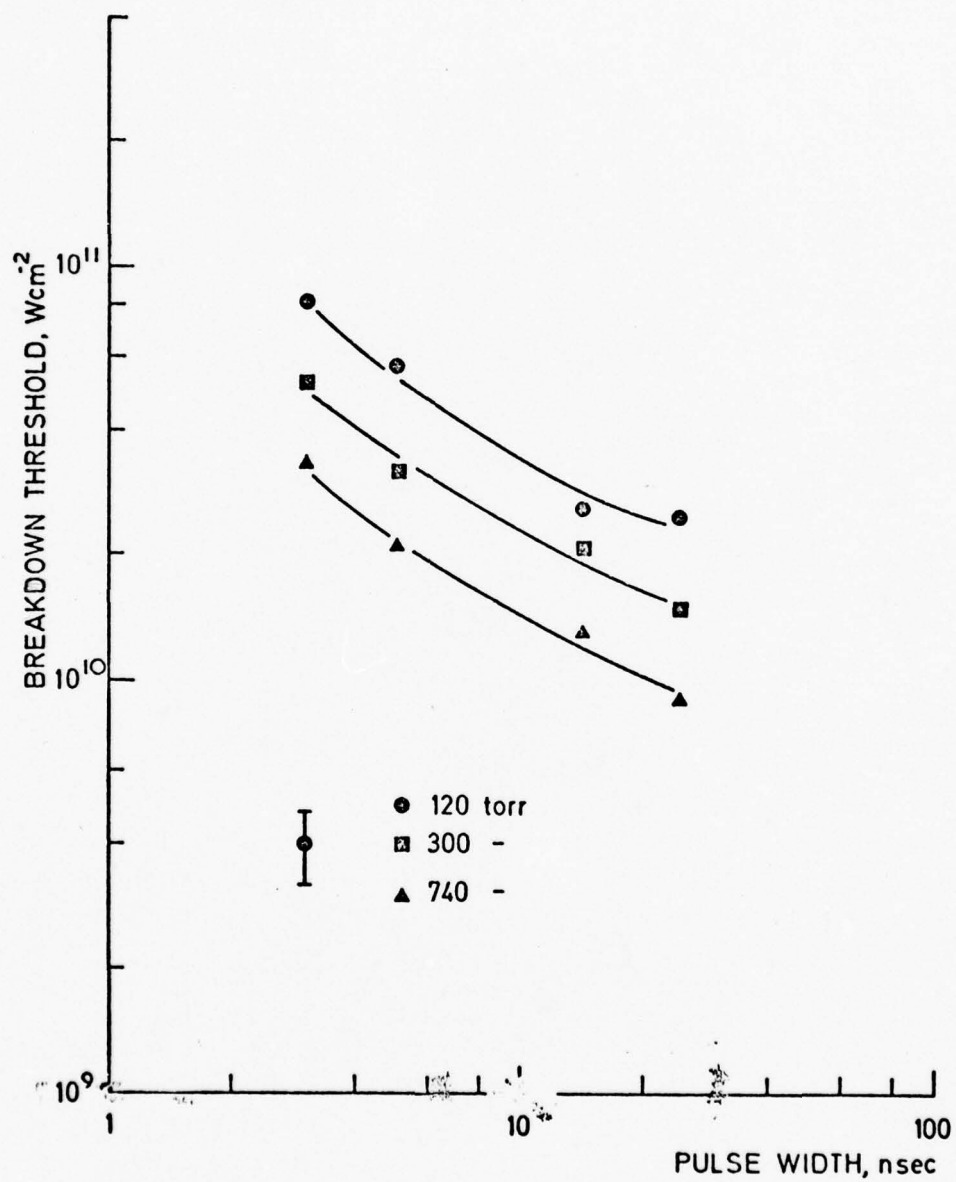


Fig 8

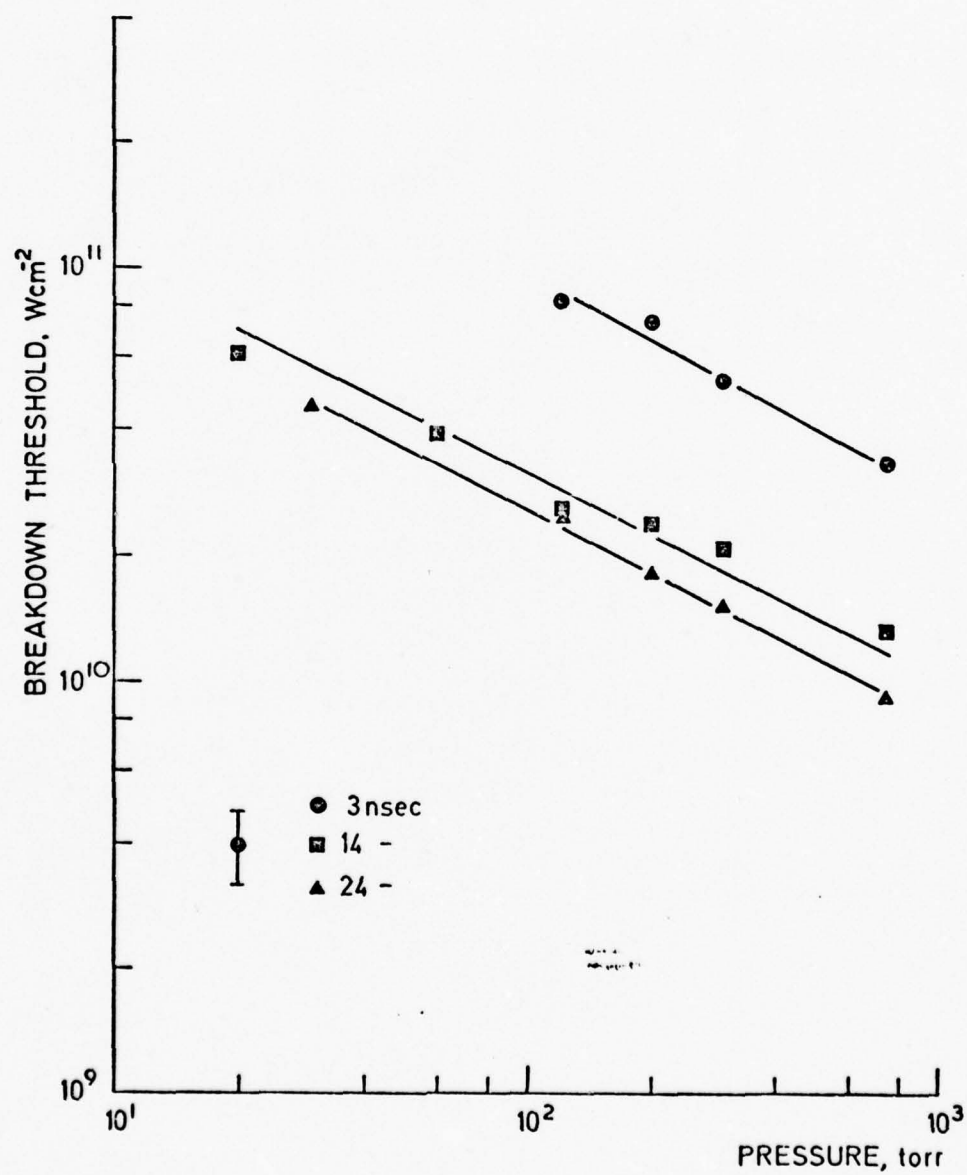


Fig 9

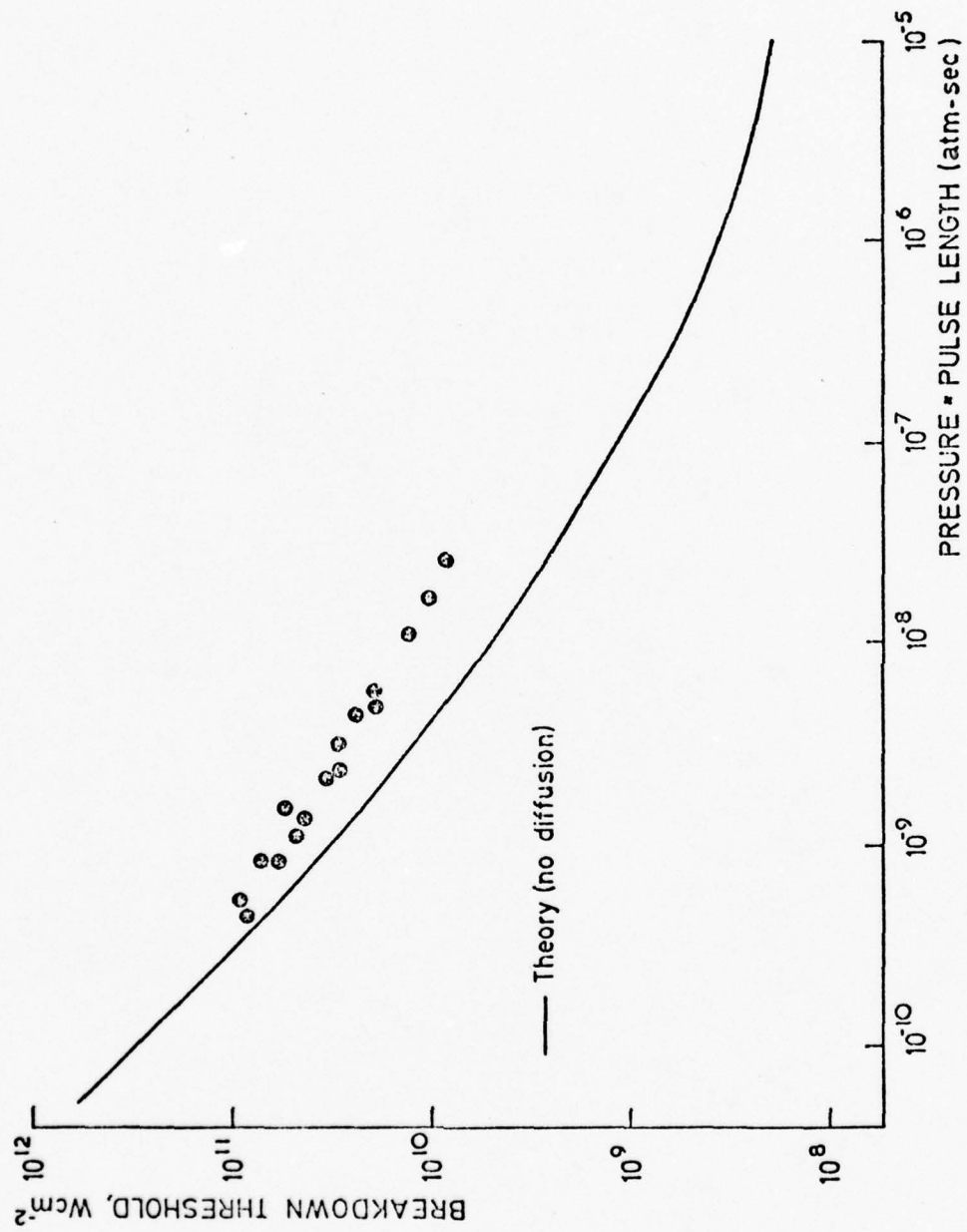


Fig 10

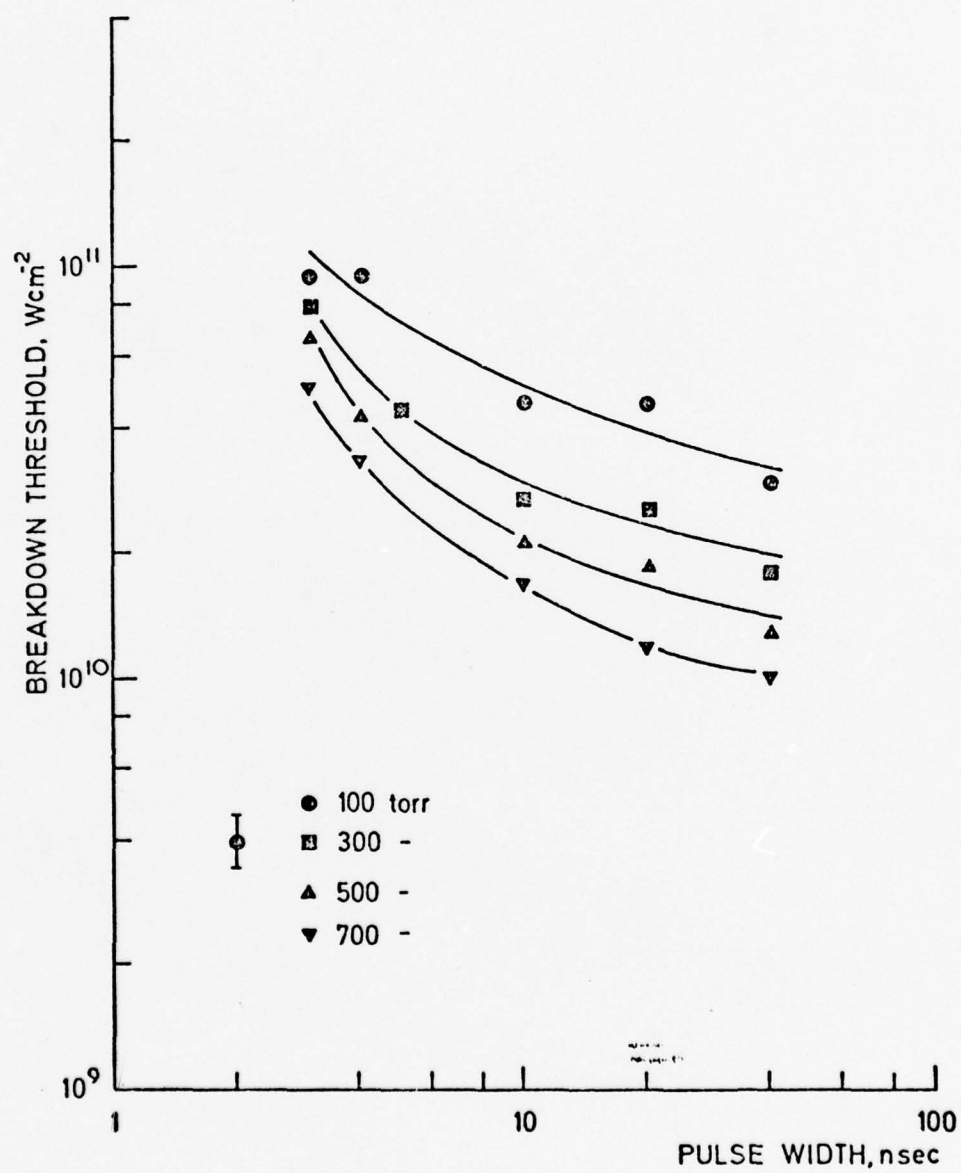


Fig 11

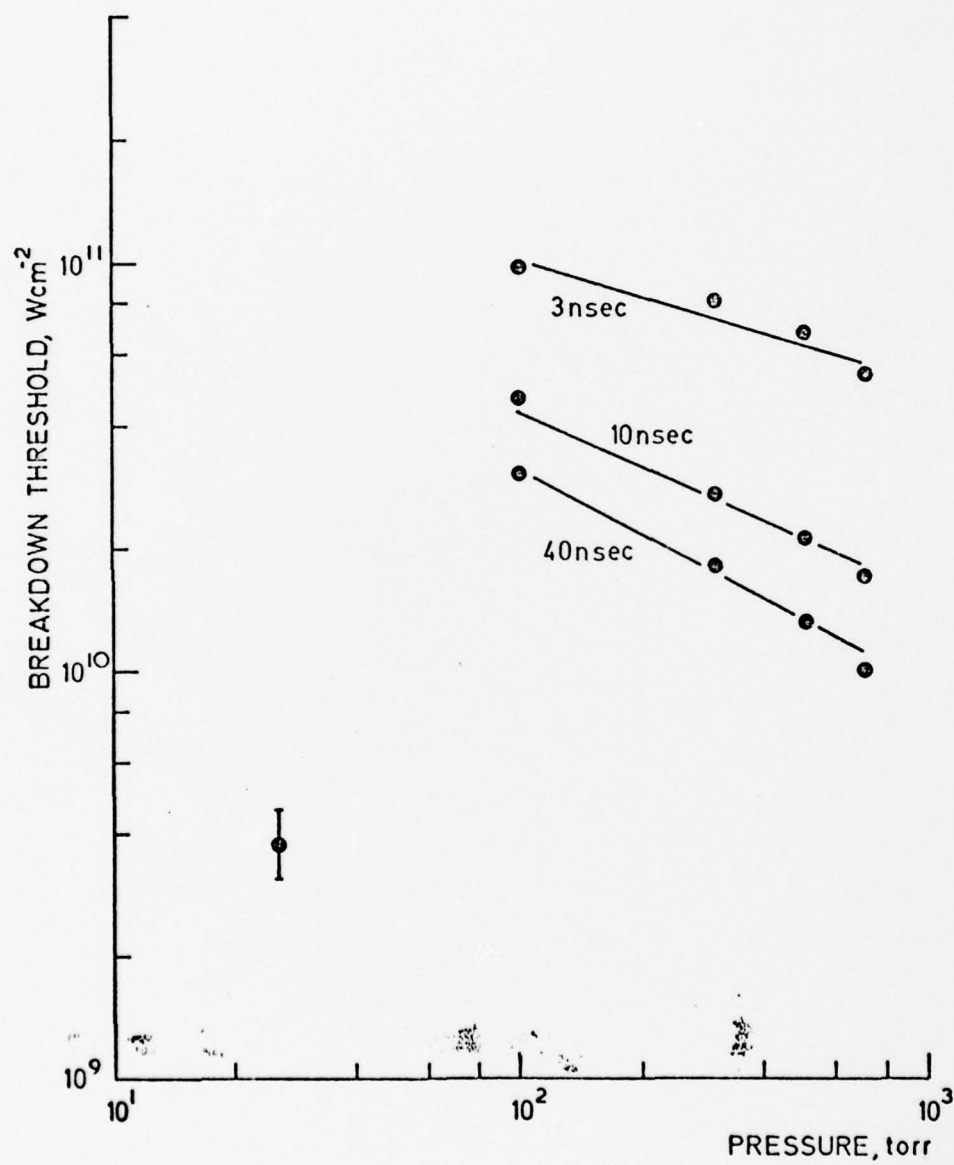


Fig 12

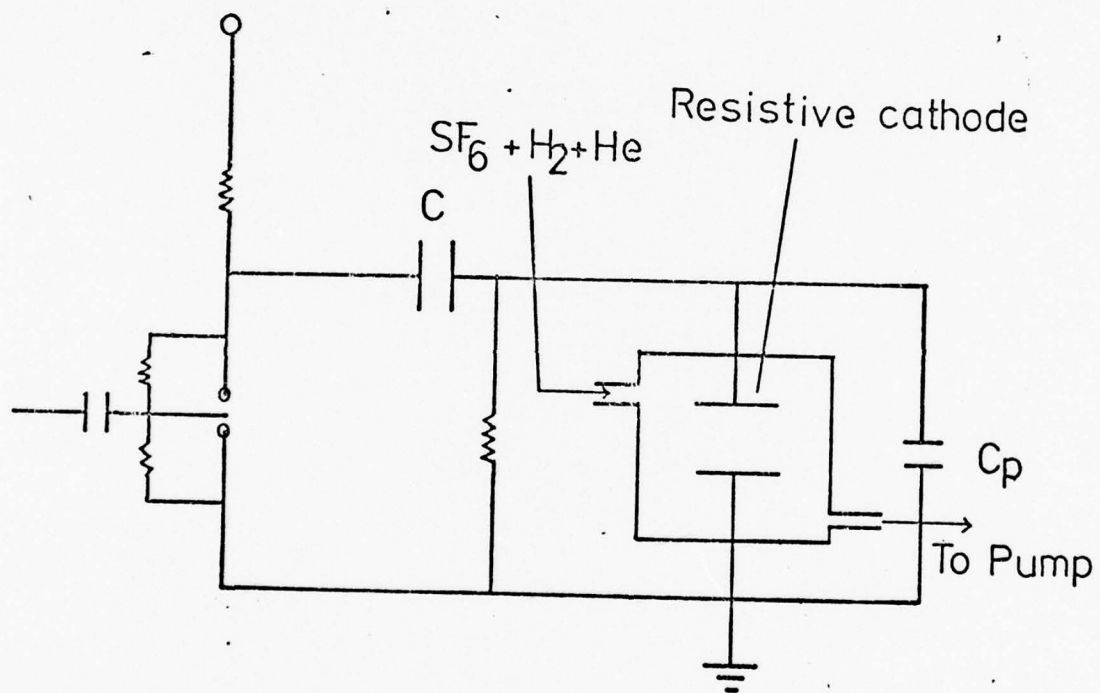


Fig 13

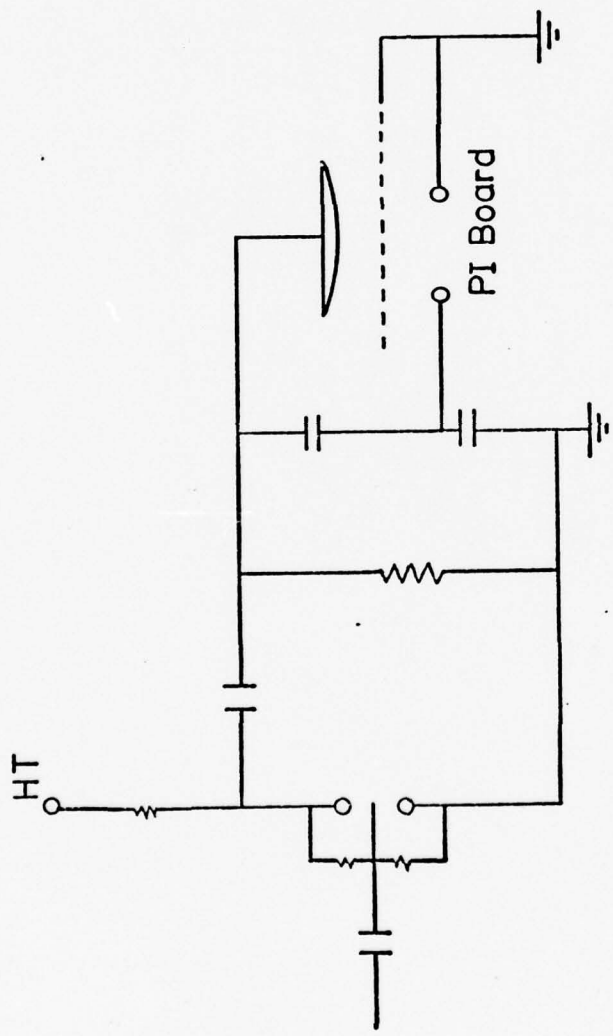


Fig 14

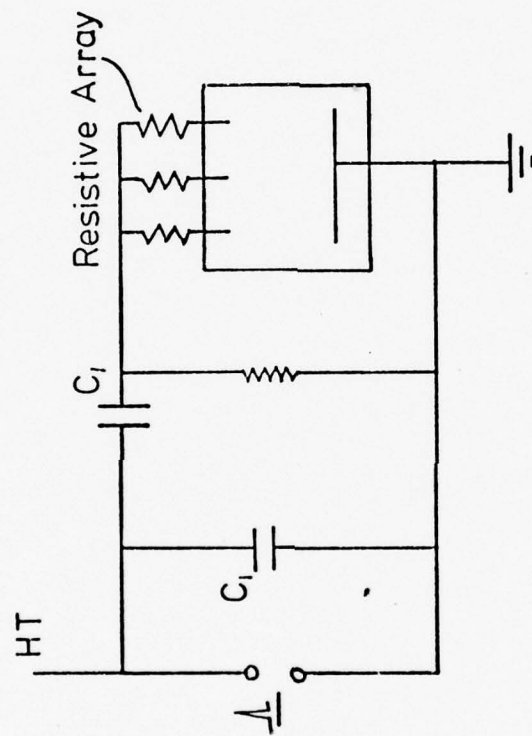


Fig 15

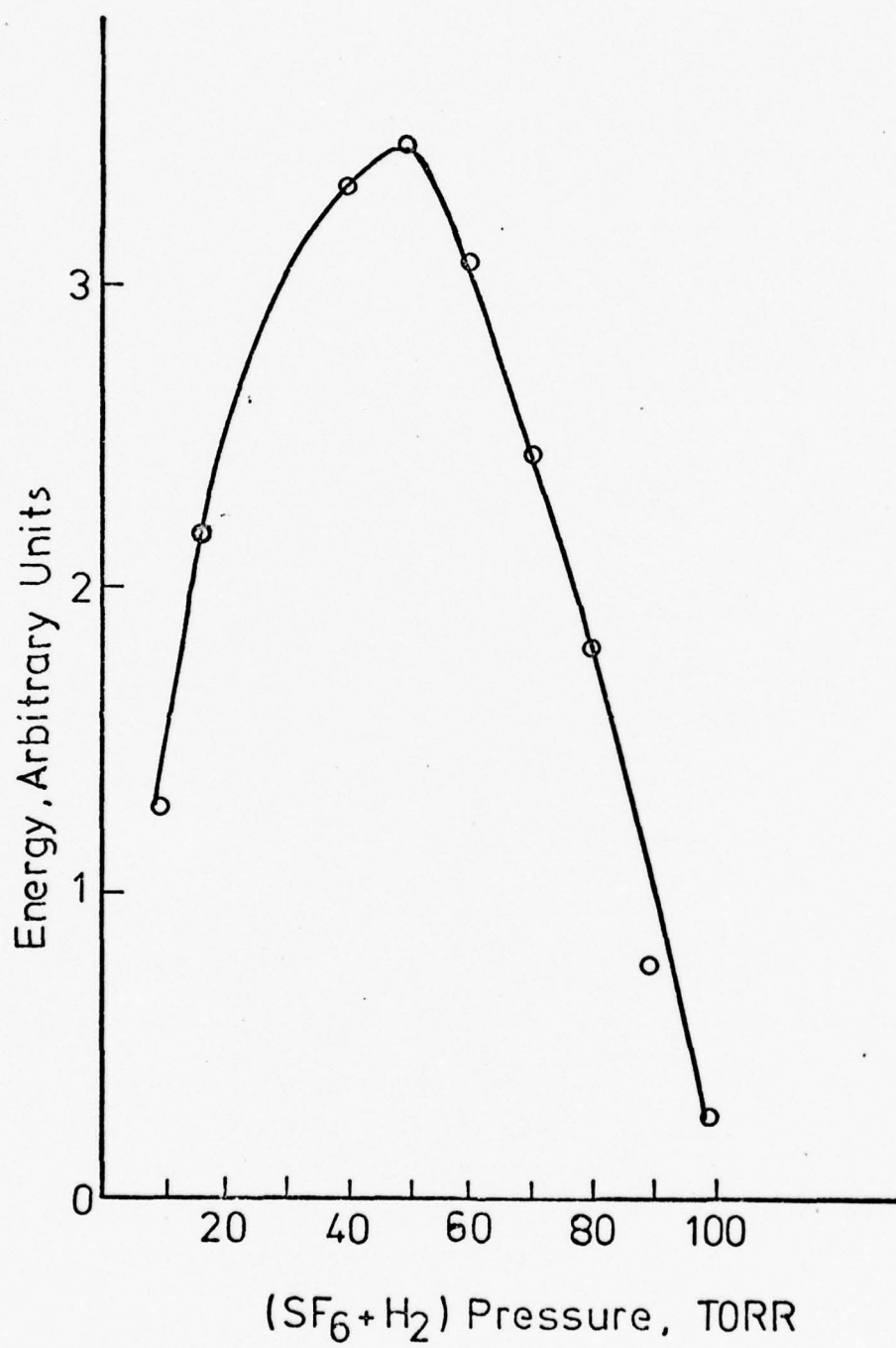


Fig 16

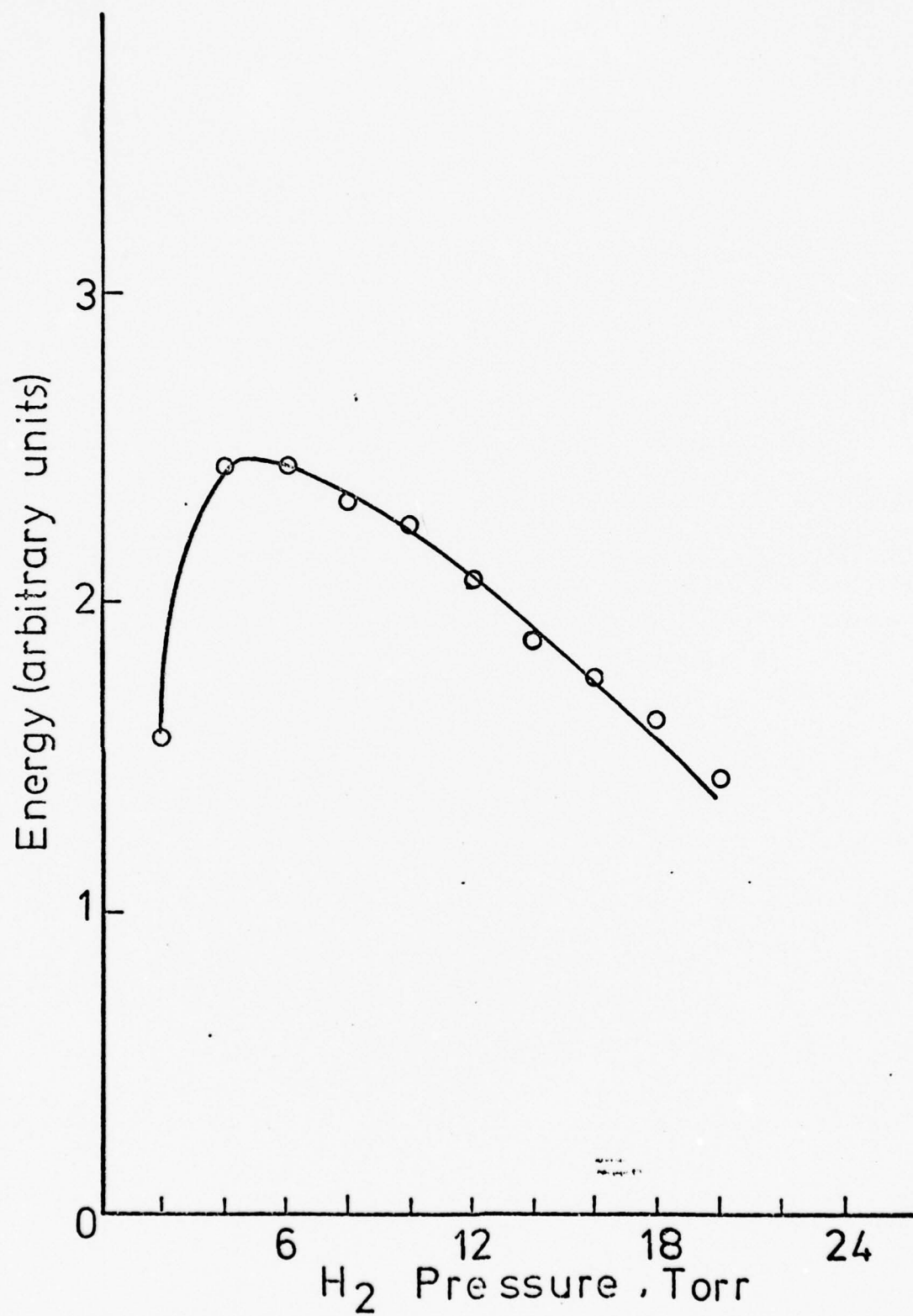


Fig 17

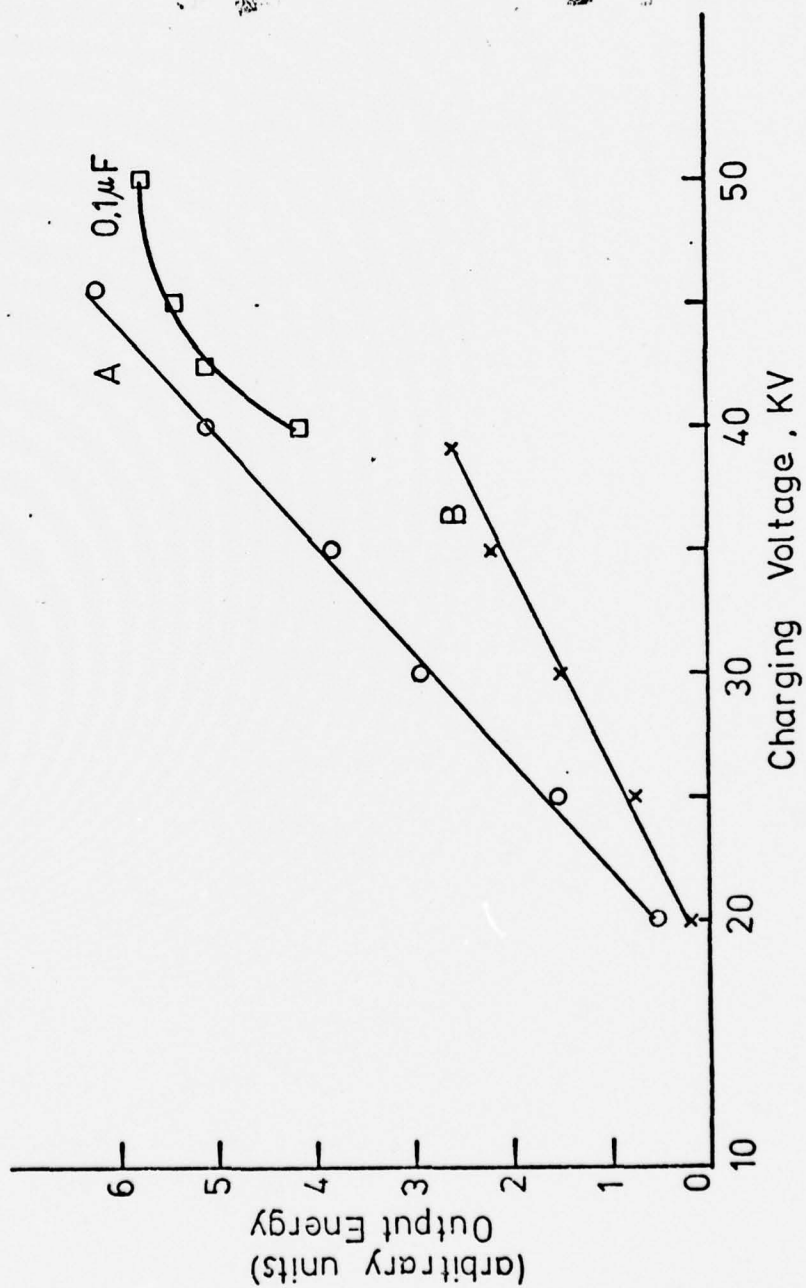
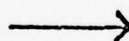
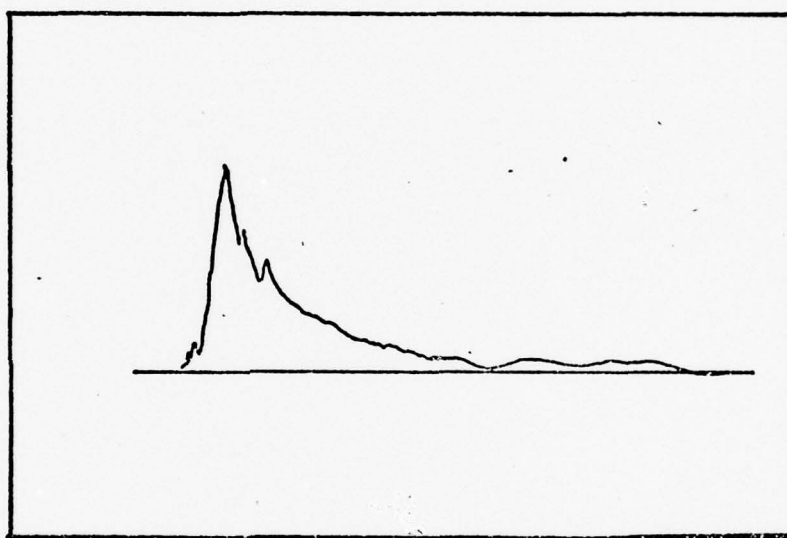


Fig 18



┌
200 ns.

Fig 19

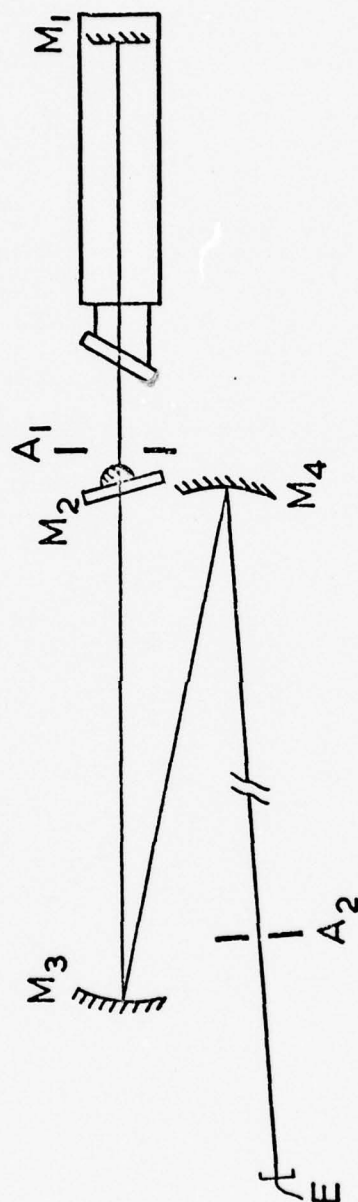
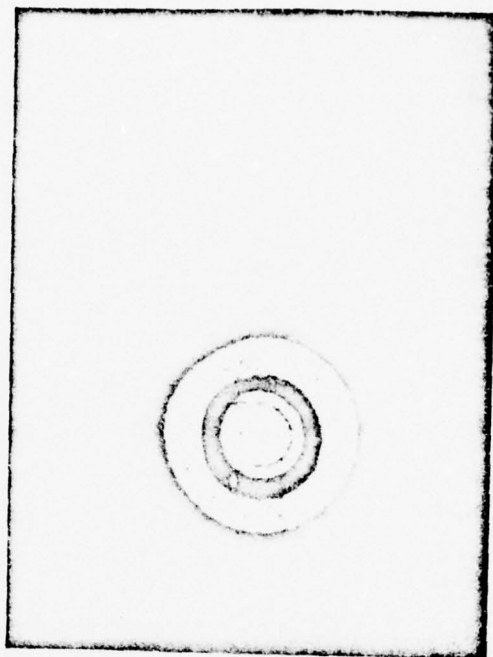
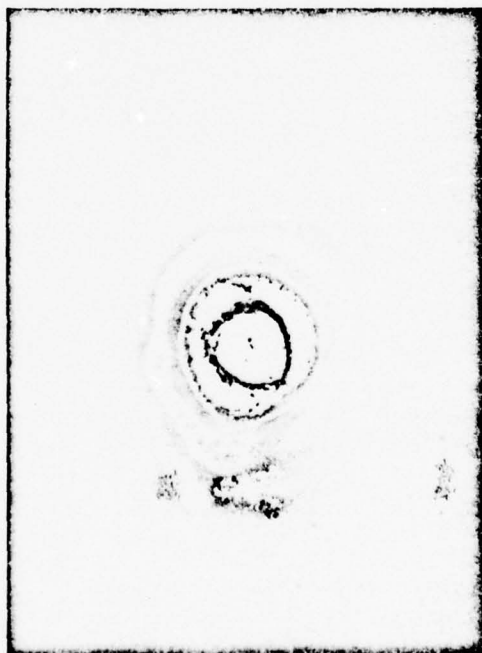


Fig 20



a)



b)

Fig 21

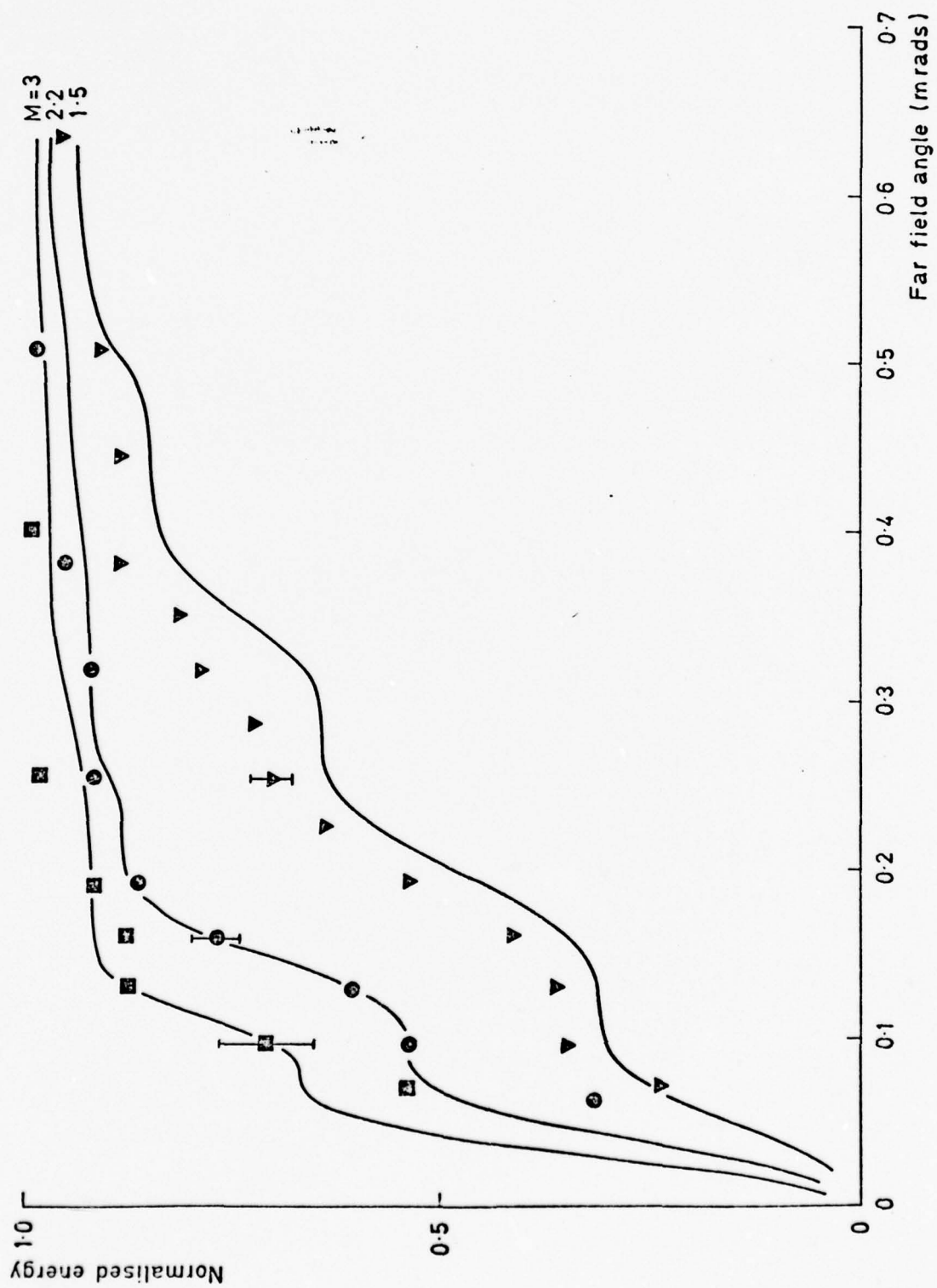


Fig 22

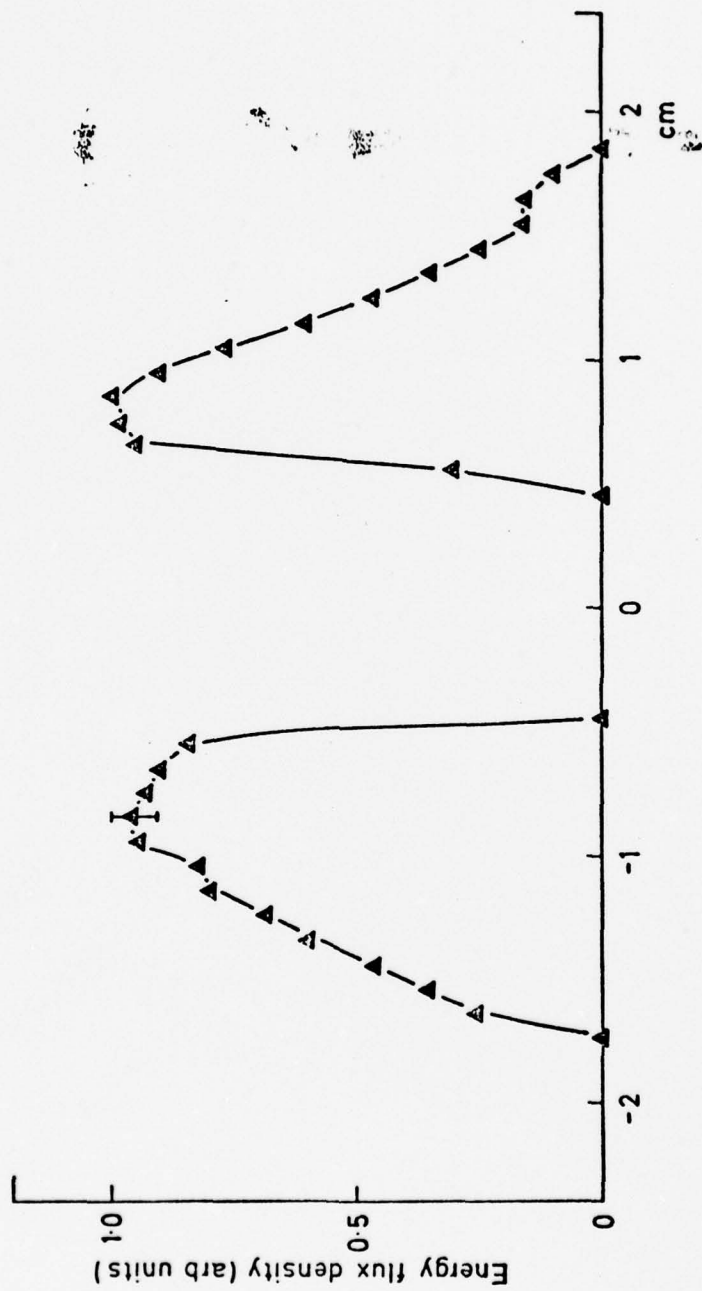


Fig 23

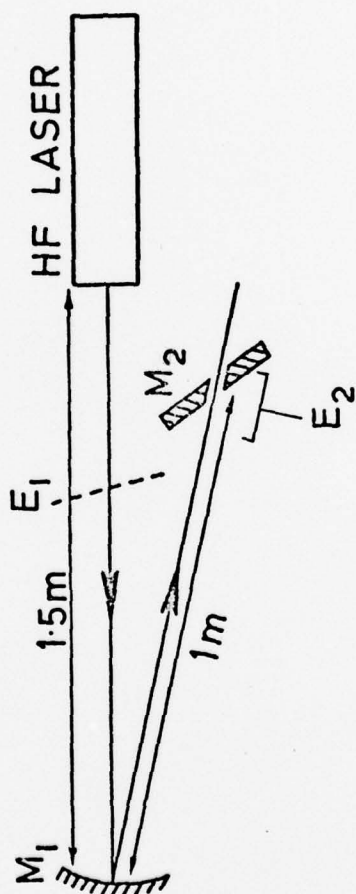


Fig 24

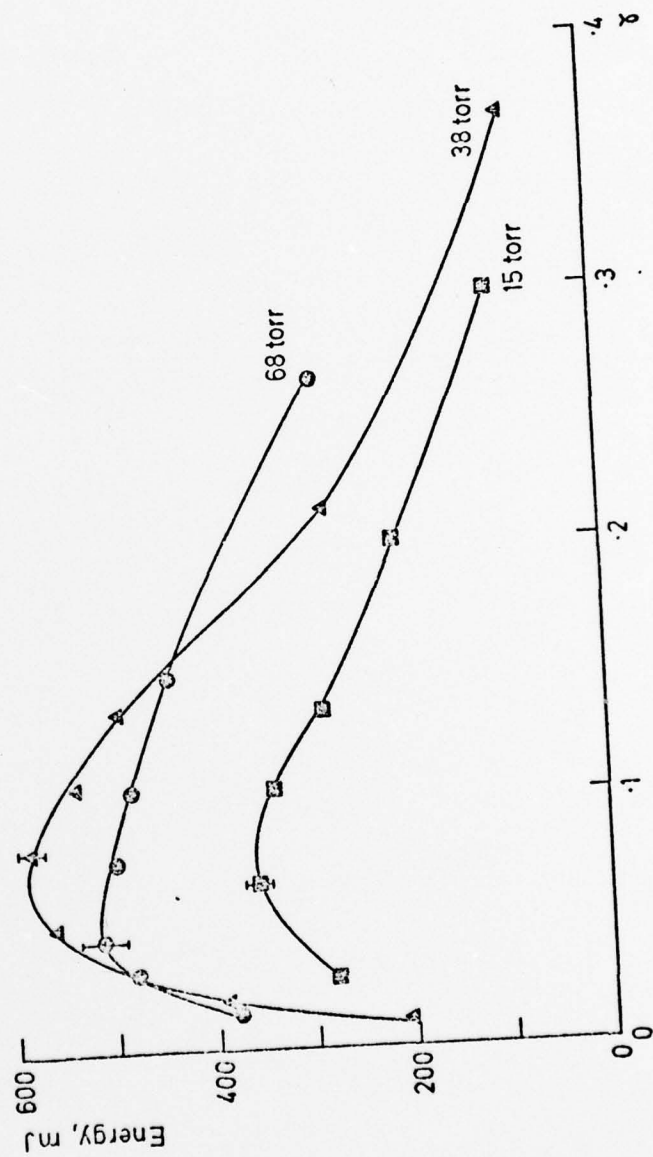


Fig 25(a)

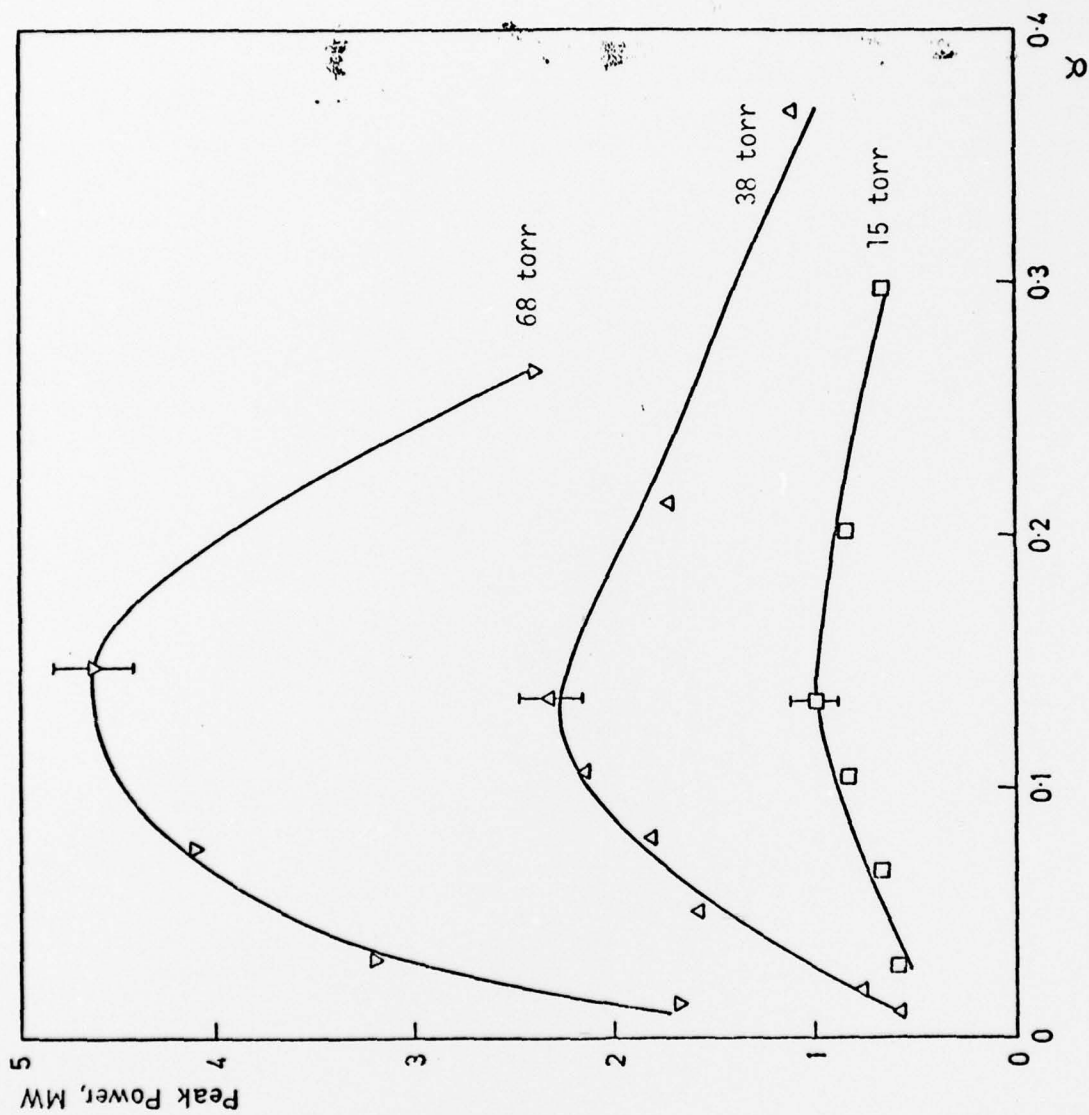


Fig 25(b)

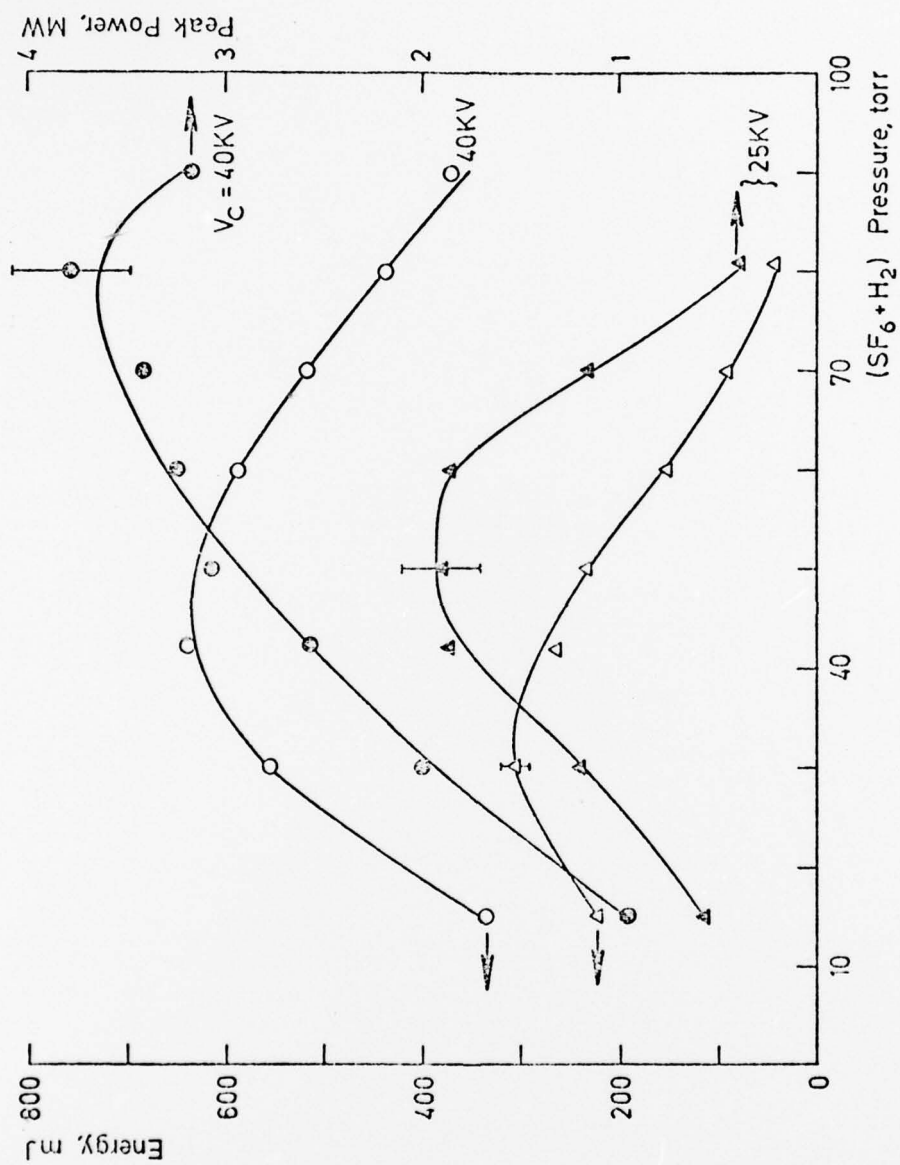


Fig 26

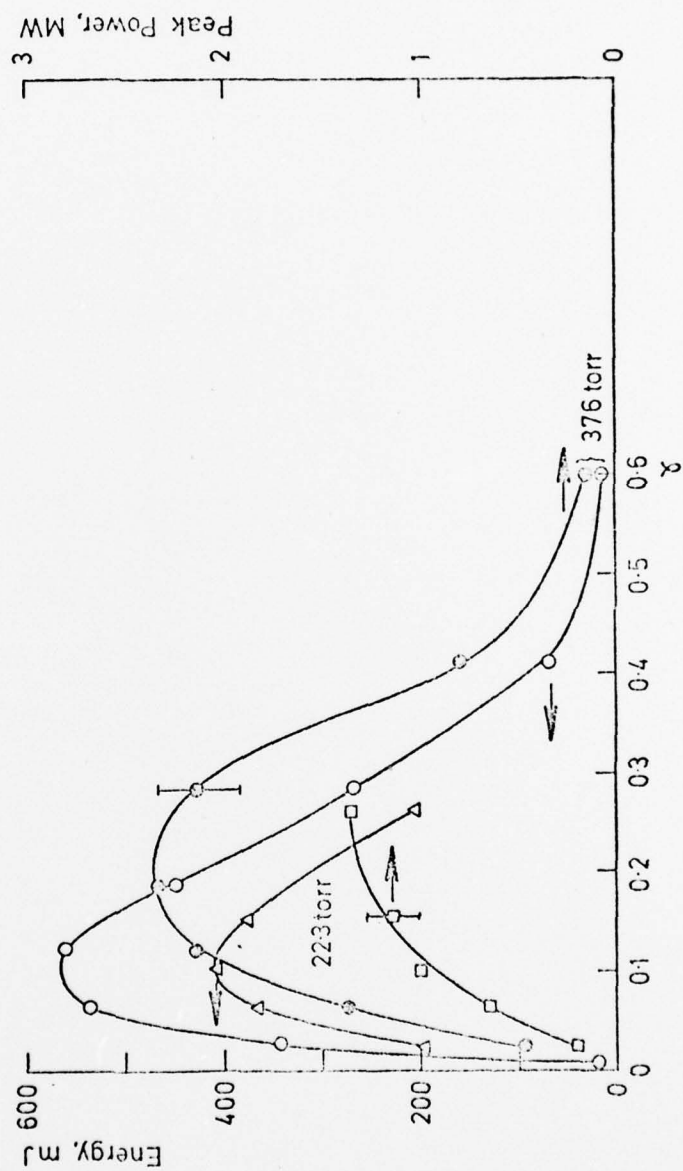


Fig 27

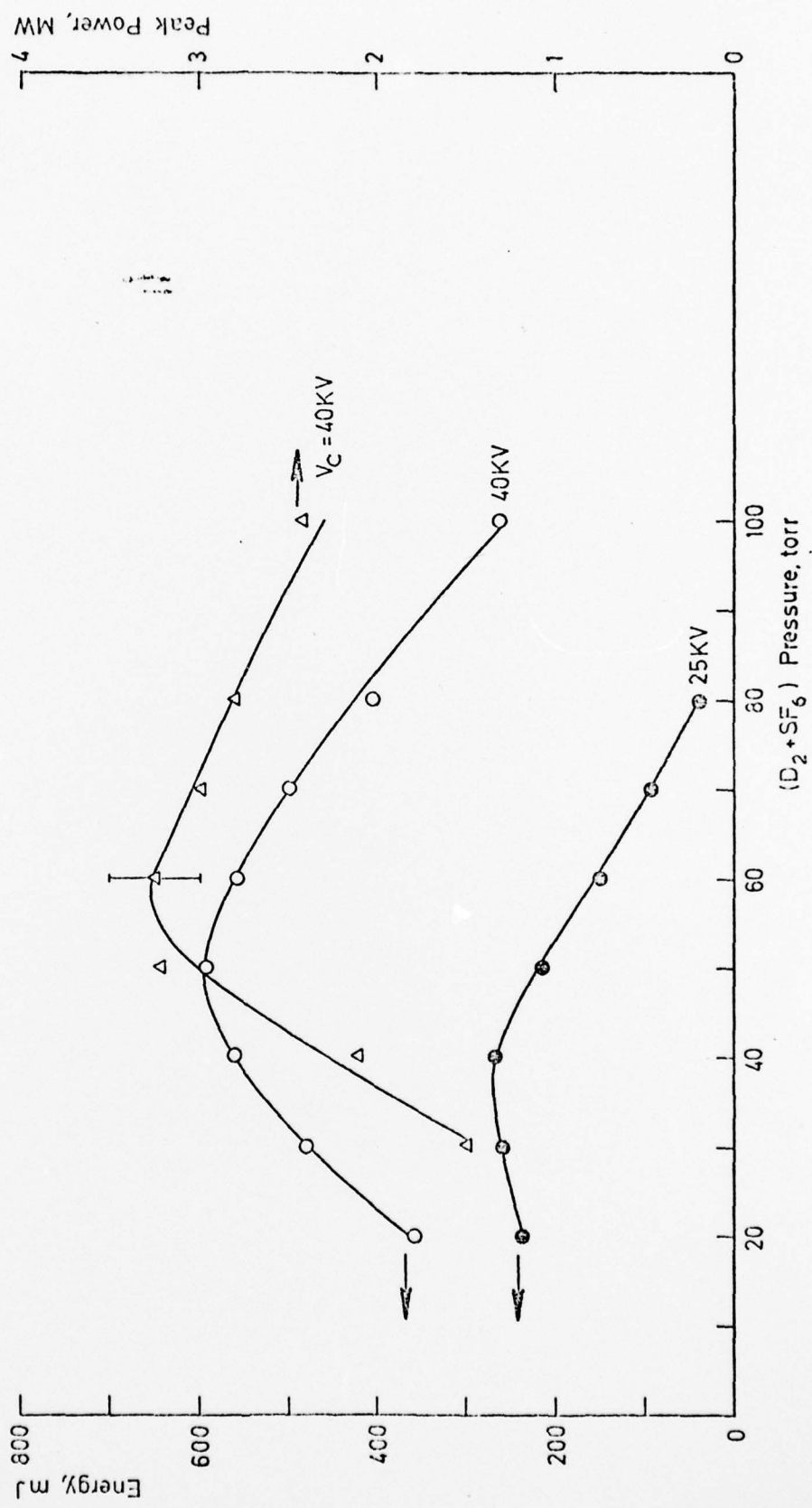


Fig 28

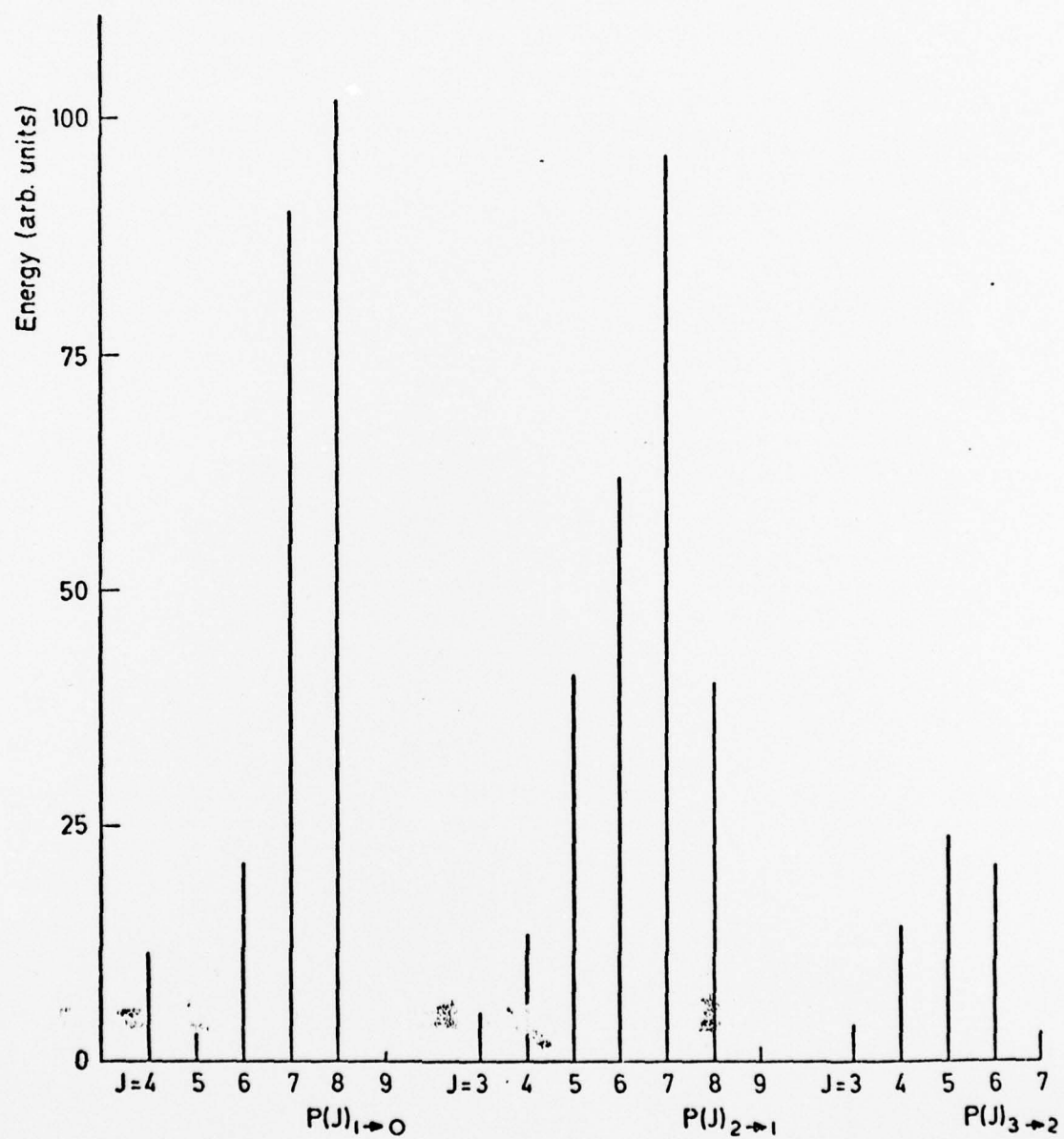


Fig 29

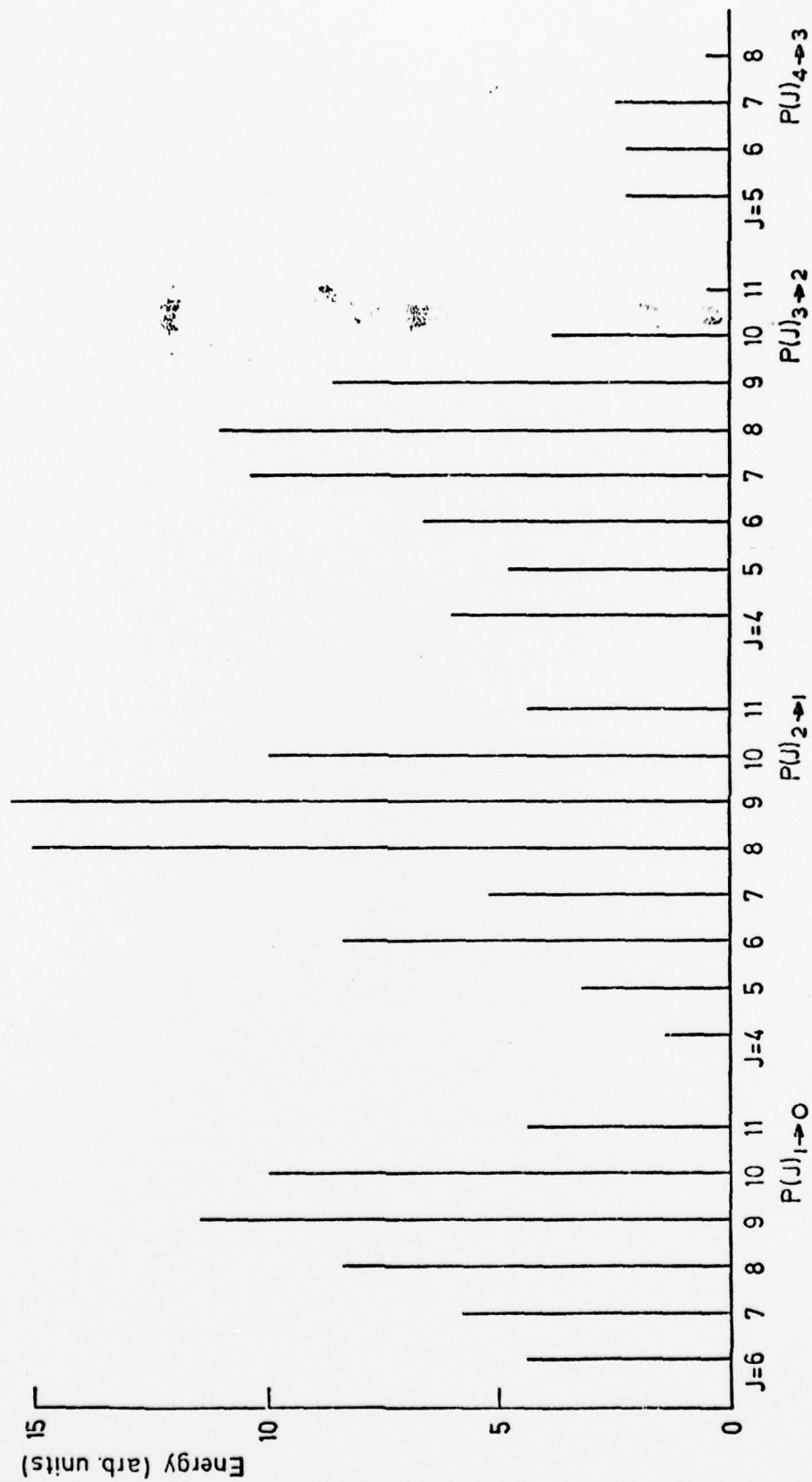


Fig 30

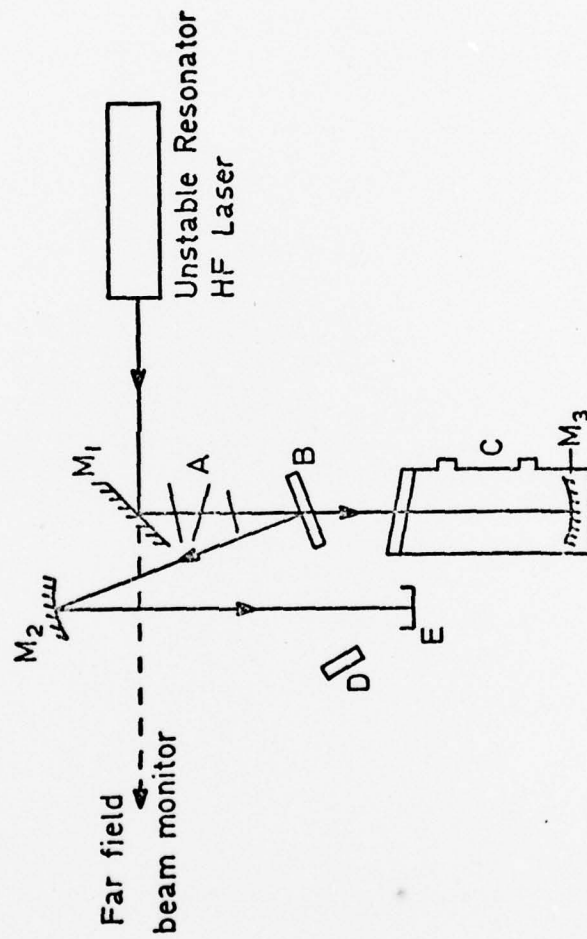


Fig 31

(a) HF



(b) DF



┌
└ 200ns

Fig 32

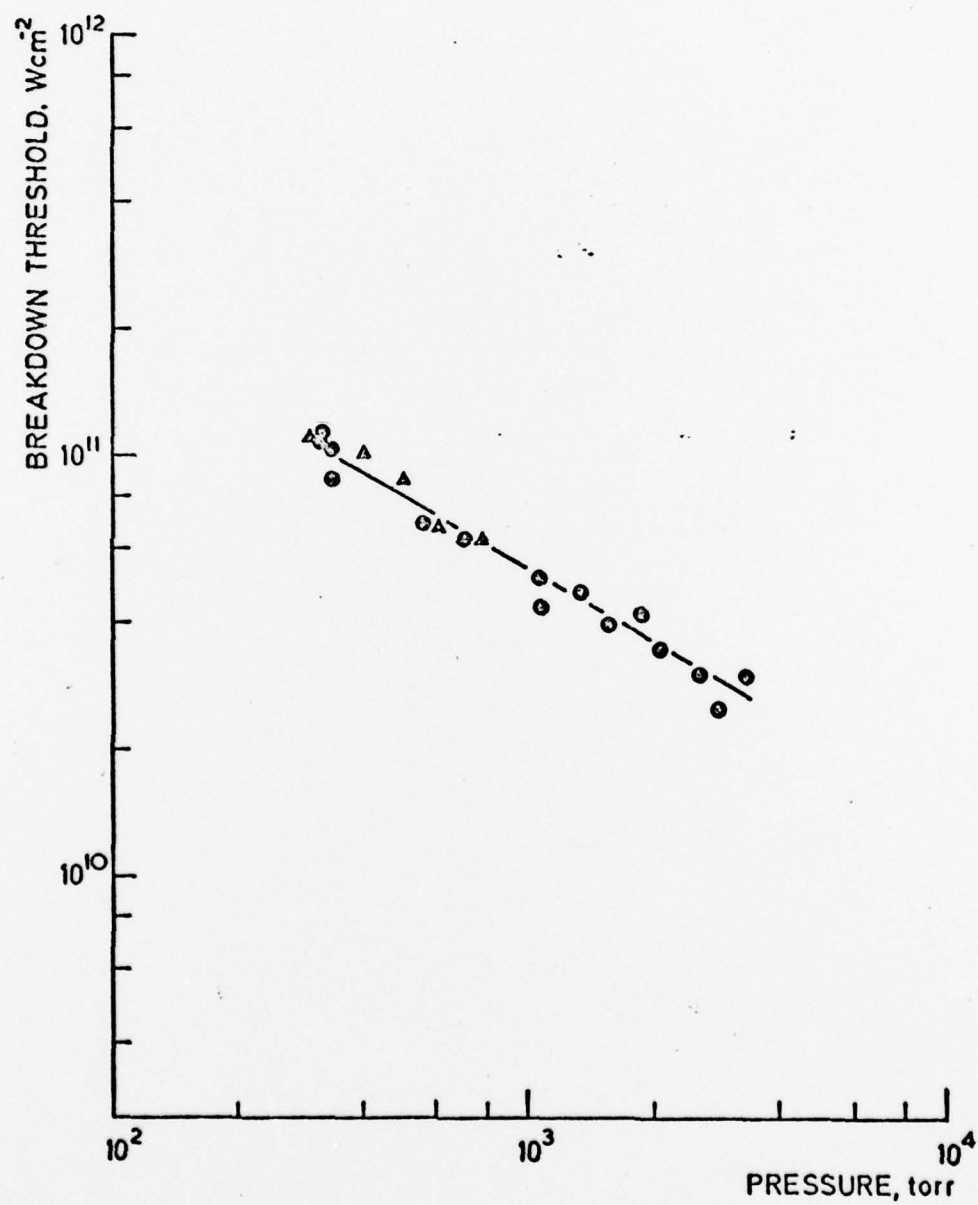


Fig 33

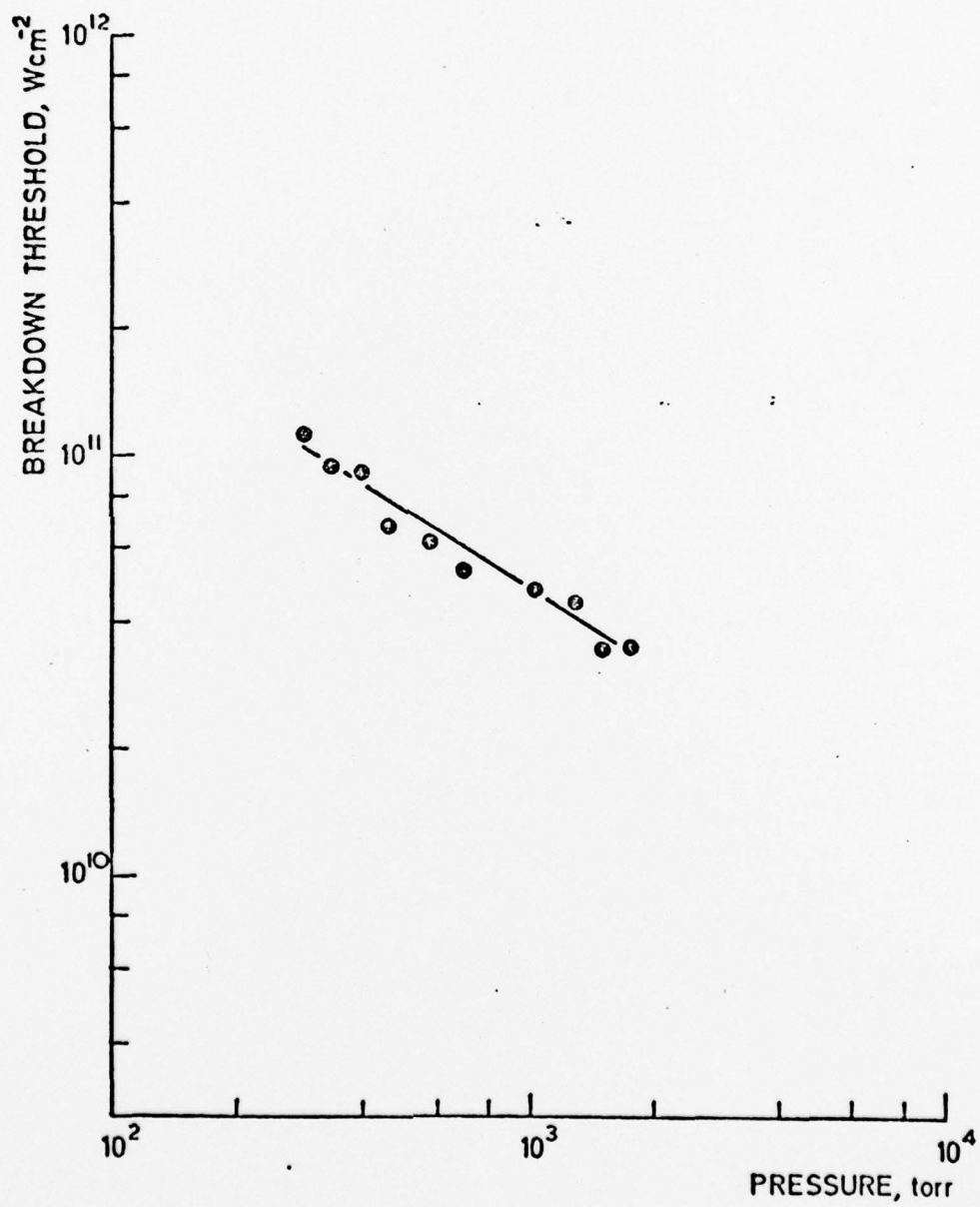


Fig 34

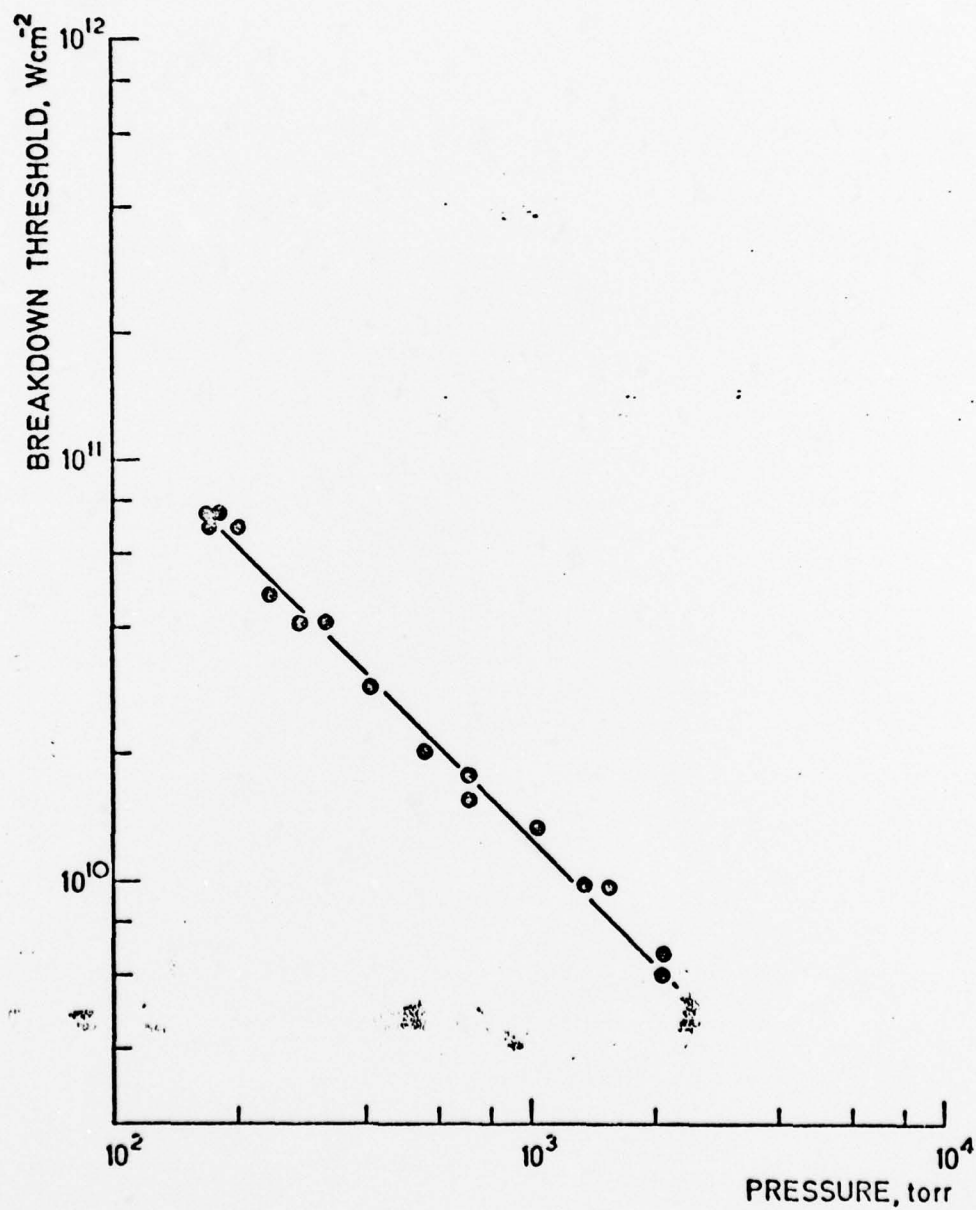


Fig 35

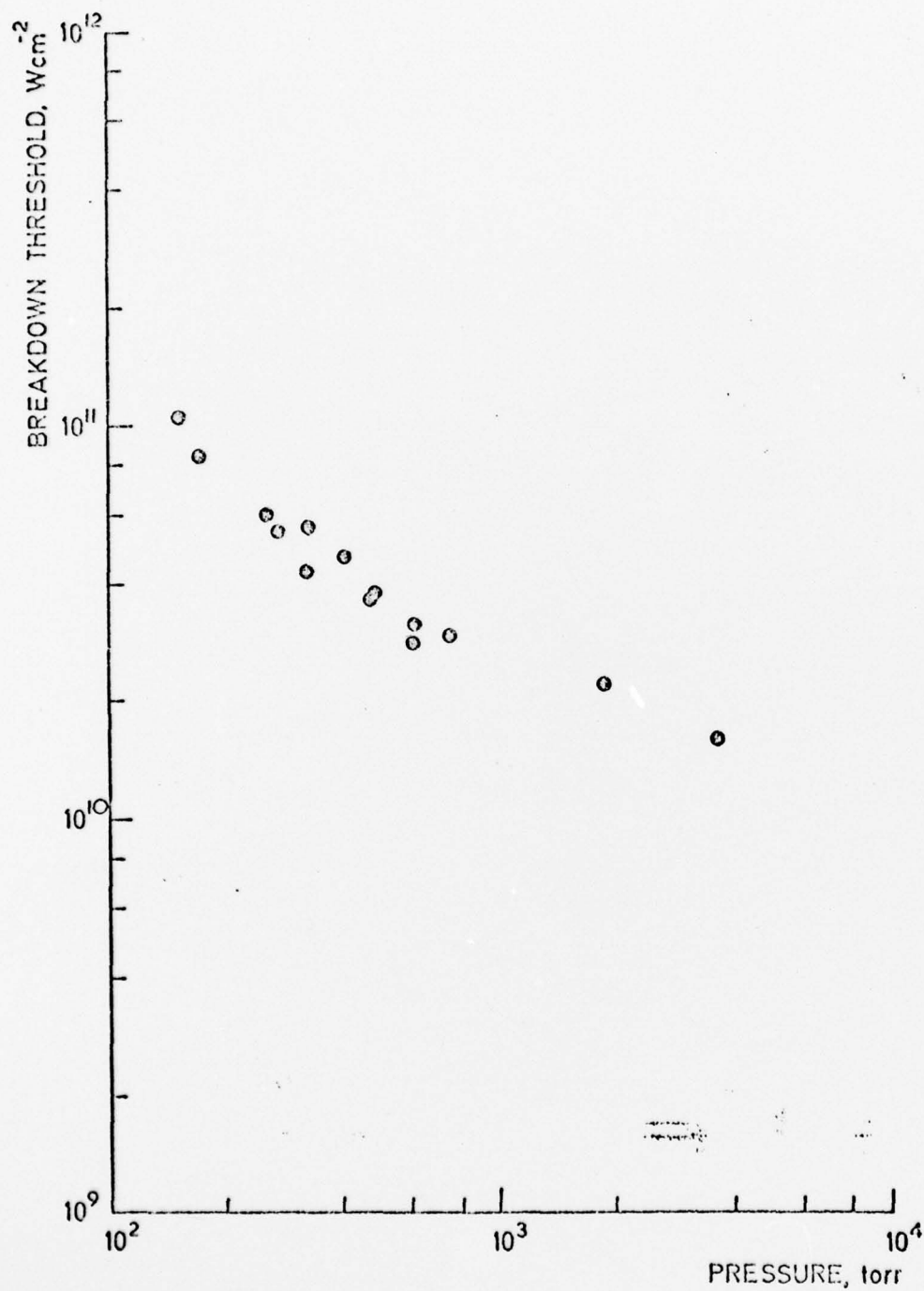


Fig 36